JGR Solid Earth

RESEARCH ARTICLE
10.1029/2021JB023587

Array Signal Processing on Distributed Acoustic Sensing Data: Directivity Effects in Slowness Space

Sven Peter Näsholm[1,2], Kamran Iranpour[1], Andreas Wuestefeld[1], Ben D. E. Dando[1], Alan F. Baird[1], and Volker Oye[1,3]

[1]NORSAR, Kjeller, Norway, [2]Department of Informatics, University of Oslo, Oslo, Norway, [3]Department of Geosciences, University of Oslo, Oslo, Norway

Key Points:

- We model directional sensitivity and gauge length effects on distributed acoustic sensing systems using array signal processing theory
- We provide closed-form expressions to estimate the steered response in slowness or wavenumber space for a given gauge length setting
- The frameworks can also be used to in some extent compensate for the directivity which varies along a geometrically non-linear cable layout

Supporting Information:

Supporting Information may be found in the online version of this article.

Correspondence to:

S. P. Näsholm,
peter@norsar.no

Citation:

Näsholm, S. P., Iranpour, K., Wuestefeld, A., Dando, B. D. E., Baird, A. F., & Oye, V. (2022). Array signal processing on distributed acoustic sensing data: Directivity effects in slowness space. *Journal of Geophysical Research: Solid Earth*, *127*, e2021JB023587. https://doi.org/10.1029/2021JB023587

Received 5 NOV 2021
Accepted 16 JAN 2022

Author Contributions:

Conceptualization: Sven Peter Näsholm, Kamran Iranpour, Andreas Wuestefeld, Ben D. E. Dando, Alan F. Baird, Volker Oye
Formal analysis: Sven Peter Näsholm, Kamran Iranpour
Methodology: Sven Peter Näsholm, Kamran Iranpour
Supervision: Andreas Wuestefeld, Volker Oye
Validation: Sven Peter Näsholm, Kamran Iranpour, Andreas Wuestefeld, Ben D. E. Dando, Alan F. Baird, Volker Oye

Abstract Distributed Acoustic Sensing (DAS) involves the transmission of laser pulses along a fiber-optic cable. These pulses are backscattered at fiber inhomogeneities and again detected by the same interrogator unit that emits the pulses. Elastic deformation along the fiber causes phase shifts in the backscattered laser pulses which are converted to spatially averaged strain measurements, typically at regular fiber intervals. DAS systems provide the potential to employ array processing algorithms. However, there are certain differences between DAS and conventional sensors. While seismic sensors typically record the directional particle displacement, velocity, or acceleration, the DAS axial strain is inherently proportional to the spatial gradient of the axial cable displacement. DAS is therefore insensitive to broadside displacement, for example, broadside P-waves. In classical delay-and-sum beamforming, the array response function is the far-field response on a horizontal slowness (or wavenumber) grid. However, for geometrically non-linear DAS layouts, the angle between wavefront and cable varies, requiring the analysis of a steered response that varies with the direction of arrival. This contrasts with the traditional array response function which is given in terms of slowness difference between arrival and steering. This paper provides a framework for DAS steered response estimation accounting also for cable directivity and gauge-length averaging – hereby demonstrating the applicability of DAS in array seismology and to assess DAS design aspects. It bridges a gap between DAS and array theory frameworks and communities, facilitating increased employment of DAS as a seismic array, while providing building blocks for the development of DAS array design tools.

Plain Language Summary This study considers optical fiber sensors to probe seismic waves. Laser light is emitted into the cable. Processing the signals encoded in the light returning back to the transmitter, we can resolve the effect of seismic waves on the cable. However, the optical cable is insensitive to waves arriving from broadside to the cable and the sensitivity is reduced for waves not arriving along the cable axis. Hence, there is a directional sensitivity to consider in the signal processing and in assessing the wavefield probing capability. This sensitivity depends on the cable layout geometry. In classical array processing with conventional sensors, the directivity is typically equal for all sensors. Here, the array response – a function of the array sensor layout – can be utilized to estimate the array's capability to resolve the direction of arrival of seismic waves. We demonstrate how to take this cable directivity into account when assessing the distributed optical sensing system direction of arrival resolution. Our tools can be applied when assessing cable layouts. In this work, we bridge the gap between classical array signal processing and the emerging field of distributed acoustical sensing system signal processing, allowing well-established processing tools to be applied.

1. Introduction

This paper considers directional sensitivity aspects of distributed fiber-optic acoustic sensing (DAS) cables employed to probe seismic waves. We provide a unified framework that bridges classical array seismology with DAS array processing to be applied by experts as well as novices from these disciplines.

Array-based methods have been used in seismology since the late 1950s and were adapted from radio astronomy, radar, acoustics, and sonar (Schweitzer, 2014). Seismic arrays (e.g., Rost & Thomas, 2002, 2009; Schweitzer et al., 2021) have the benefit of both improving the signal-to-noise ratio (SNR) of a seismic phase onset, whilst also providing information on the direction-of-arrival for an incoming signal. Applications of seismic arrays are wide ranging and include the monitoring of nuclear explosions, analyzing volcanic tremors, determining earth structure, and more recently, monitoring of induced seismicity (Oye et al., 2021).

Visualization: Sven Peter Näsholm, Kamran Iranpour, Andreas Wuestefeld
Writing – original draft: Sven Peter Näsholm, Kamran Iranpour, Andreas Wuestefeld
Writing – review & editing: Sven Peter Näsholm, Kamran Iranpour, Andreas Wuestefeld, Ben D. E. Dando, Alan F. Baird, Volker Oye

A seismic array is a collection of spatially distributed sensors. Typically, the array element traces are processed collectively through a stacking procedure, rather than treated as individual signals. For a distant source, the incoming wavefield should be spatially coherent across the array, lending itself to advantageous signal processing routines that can serve as spatial filters to focus the reception toward a preferred direction-of-arrival. Array-based signal processing techniques include variations of delay-and-sum beamforming (implemented in either the temporal or frequency domain) including the evaluation of the array output as a function of direction-of-arrival (often mapped to its corresponding horizontal slowness components, wavenumber components, or using a backazimuth and trace velocity parameterization). These methods typically extract both the coherency and the directivity information that can be derived from array observations (see, e.g., Krim & Viberg, 1996; Uncini, 2015; van Trees, 2004, for overviews and fundamental array signal processing theory). From a processing efficiency perspective, it is often convenient to implement the algorithms in the frequency-wavenumber (f–k) domain where time-delaying a signal corresponds to multiplication by a phase factor, rather than performing the calculations in the time domain (Capon, 1969). The f–k family of implementations have also been extended to allow for broadband signal analysis (Gal et al., 2014; Kvaerna & Doornbos, 1986). In array seismology, the term f–k analysis is sometimes used in a more general sense to refer to any estimation of array output as a function of slowness and its display on a two-dimensional (s_x, s_y) grid.

The instrumentation used for seismic arrays have traditionally been single or three-component broadband seismometers. In the case of targeting higher frequency signals with a requirement for portability, geophone arrays have proved a cheaper and more flexible alternative. For single-component instruments, the sensor directly measures changes in ground motion along one direction, at a specific location. For three-component instruments the combination of sensors probe the ground motion in all directions, also at a specific location.

DAS is an alternative type of instrumentation based on detecting localized deformation of a fiber-optic cable, which in the context of seismology could be caused by a passing seismic wave. A laser pulse is transmitted along the fiber, where randomly distributed inhomogeneities cause Rayleigh backscattering, which are then detected by an interrogator unit. Changes in the phase of the backscattered light are proportional to any fiber deformation that occurs, allowing the strain-rate to be measured at high spatial and temporal resolution along the length of the fiber (Zhan, 2020). At present, measurements have been made up to 171 km along a fiber (Waagaard et al., 2021), demonstrating the potential for cable deployments capable of monitoring a broad range of length scales.

Although single-mode optical fibers have been in use since the early 1960s, the use of Rayleigh-backscattered light for the purposes of DAS was established only within the last two decades. DAS has a diverse set of applications which extend beyond traditional seismological monitoring. These include borehole monitoring of subsurface reservoirs using active seismic (Daley et al., 2016), microseismic monitoring of hydraulic fracture stimulations (Baird et al., 2020), glacial microseismicity (Hudson et al., 2021; Walter et al., 2020), time-lapse monitoring using the ambient noise field (Dou et al., 2017), urban ambient noise characterization (Zhao & Li, 2020), border control and security applications (Juarez & Taylor, 2007), onshore pipeline monitoring (Tejedor et al., 2017) and railway and highway monitoring (e.g., Chambers, 2020; Peng et al., 2014).

Moreover, the extensive infrastructure of unutilized telecommunication fiber provides huge potential for various geophysical monitoring applications (e.g., Ajo-Franklin et al., 2019) with even existing underwater cables able to be repurposed for monitoring in challenging marine environments (Lior et al., 2021; Williams et al., 2019). Optical cable-based systems have also been employed in atmospheric acoustics related studies, for example, looking at thunder-induced ground motion using DAS (Zhu & Stensrud, 2019). Even without exploiting the array sensing opportunities offered by DAS, optical cables can be used for a wide range of geophysical investigations, for example, as demonstrated in atmospheric infrasound studies (Costley et al., 2013; Zumberge et al., 2003) and in detecting ocean waves and seismic shaking (Zhan et al., 2021).

Given the great flexibility in how and where a fiber-optic cable can be deployed, the extent along a cable for which measurements can be made, and that the sensors are distributed along its length, there is significant potential for using DAS for seismic array processing. As such, several very recent studies have analyzed various aspects of applying beamforming algorithms to DAS array measurements. van den Ende and Ampuero (2021) compared the beamforming performance for a DAS array to the performance of a co-located conventional array, finding that the DAS array provided excellent localization of a regional earthquake, albeit with a decreased waveform coherence compared to the conventional array. Nayak et al. (2021) exploited a large-aperture DAS configuration, which

in the signal processing pipeline was forked into several sub-arrays, for which individual beamforming recipes were applied to generate one short-term/long-term average detection statistic for each sub-array. These were then piped into a voting detector that was capable of detecting minor earthquakes with great accuracy. Further, it was shown by Nayak et al. (2021) that DAS beam-power could be used to discriminate between phase arrivals using time-slowness vespagrams for 2 km aperture sub-arrays. Paitz et al. (2019) investigated the relations between the wave equation solution and interferograms based on displacement, strain, or rotation. Their theory is applicable to the DAS context and can also incorporate gauge length averaging effects. Moreover, Martin et al. (2021) analyze key differences between DAS and geophone plane-wave measurements, highlighting, for example, ambient noise interferometry and inter-receiver correlation aspects. Recently, Klaasen et al. (2021) used a DAS deployment to study an active volcanic complex. They applied a beamforming recipe where only sensors with an SNR above half the maximum sensor SNR were included in the stacking, hence excluding cable segments with unfavorable direction-dependent sensitivity.

In considering array applications for DAS, one must first consider its unique signal characteristics and the implications therein. As underlined above, DAS measures the relative deformation between two material points, that is, the strain, or its temporal derivative which is the strain-rate (Rodriguez & Wuestefeld, 2020). This is fundamentally different from the single point measurements of pressure, displacement or velocity provided by microbarometers, seismometers or geophones (see Section 2) typically used for array processing. Consequently, because a DAS cable can only sense the axial component of the displacement gradient (the directional derivative), it is only sensitive to the component of propagating P-waves that is parallel to the local orientation of the cable. This sensitivity renders DAS blind for P-waves arriving broadside to the cable as well as for S-waves arriving along the axial direction.

In practice, the strain is measured over a pre-selected gauge length (Mateeva et al., 2014), which corresponds to an effective sensor length over which the average strain is estimated. Longer gauge lengths increase the signal-to-noise ratio, while a shorter gauge length reduces the spatial smearing (see Section 2.1.2) while also allowing for higher frequency waves to be recorded. The spacing of these virtual sensors, typically referred to as channels, is determined by the length of the laser pulse. Since their spacing can be smaller than the gauge length, it is also possible to have overlapping channels defined along the fiber.

Thus, to apply array processing techniques to DAS data, we must account for the inherent differences in signal type and measurement principle. The sensitivity and resolution of a seismic array to plane waves of different frequencies and slowness is traditionally assessed in terms of the array response function which is controlled by the aperture, sensor spacing, number of sensors, and overall geometry of the array. In this paper we look in detail at how DAS signals will influence the array response function. The three key features specific to DAS that determine the directional response to ground motion are: (a) the spatial layout of the virtual sensors of the array; (b) the directional sensitivity of the fiber; (c) the gauge length averaging of the strain rate measurements. This paper formulates a consolidated theory which takes these three effects into account, using well-established array processing frameworks. This allows for designing optimum array geometries and other processing and configuration aspects for DAS systems.

There are several well-established principles for design of the geometric configuration of conventional seismic arrays for coherent array signal processing. These are typically based on optimizing the array response function in terms of mainlobe and sidelobe structure for a given frequency range and set of seismic wave types (Kennett et al., 2015; Mykkeltveit et al., 1983; Mykkeltveit, Ringdal, et al., 1990; Schweitzer et al., 2012). The width of the mainlobe is related to how closely separated two impinging wavefronts can be while still being resolved by the array measurements. The sidelobe levels are typically related to the contrast resolution of the array measurements (see also Section S4 in Supporting Information S1). The goal is often to obtain high resolution in the estimated wavefront parameters, which are tightly related to resolving the directions-of-arrival of interest. Array design constraints typically lay in the number of sensors available, land access, the seismic noise characteristics, and the inter-sensor signal coherence as function of distance. The current work lays out a framework for developing mainlobe and sidelobe based analyses also in DAS array design optimization.

Incoherent processing approaches can to some extent mitigate limitations coming from decorrelation of higher-frequency arrivals (Gibbons, 2014; Gibbons et al., 2008; Kvaerna et al., 2021). Recently, efforts also have

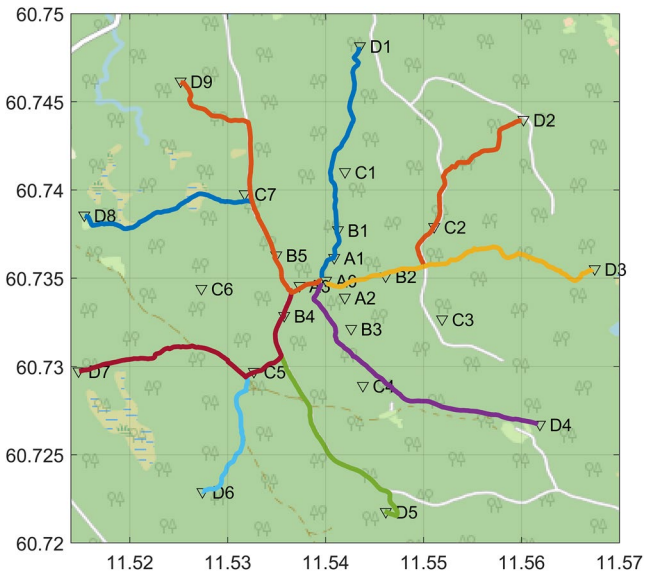

Figure 1. Map of the NORES conventional array as well as the co-located shallow buried optical fiber cable layout. The seismometer locations are shown as black triangles. Seismometers in the outer ("D-") ring (at around 1.5 km distance from the center) are currently decommissioned.

been made to mitigate slowness estimation uncertainties due to, for example, array geometry and noise structure using a sensor bootstrapping approach (Ward et al., 2021).

In the following Background Theory Section 2, we highlight key aspects of DAS-based probing and underline central array signal processing and beamforming concepts. Two sections then follow with the main novelties of this work: Section 3, Methods Developed, describes a consolidated approach to predict the total directional sensitivity of a DAS cable layout and a recipe to calculate this numerically, while the Results Section 4, applies these methods to a set of idealized DAS cable layouts, as well as to an optical fiber layout that is co-located with the NORES conventional 3-component regional seismic array in central Norway (located at 60.75°N, 11.54°E). Since the late 1980s, multi-mode optical communication fibers have been deployed at NORES in a 9-arm geometry, stretching out from the central acquisition hub to different seismic sensor sites, see Figure 1. The paper closes with a Discussion and Conclusions Section 5 where the results are put into context and suggestions for further investigations are provided. There are plans for upgrading the NORES layout to serve as a dedicated DAS array and this section discusses approaches upon which DAS array layout design rules could be developed in the future.

2. Background Theory

2.1. Distributed Acoustic Sensing Concepts

In this section, we describe fundamental distributed acoustic sensing concepts, in particular highlighting aspects important when applying beamforming recipes to DAS datasets. Cable directivity and gauge length averaging effects can be incorporated into array signal processing theory, as is later shown in Sections 3 and 4.

2.1.1. Directivity in DAS Cable Sensitivity to Strain and Particle Displacement

DAS systems measure strain or strain rate (Jousset et al., 2018), with the strain rate being the temporal derivative of strain. The infinitesimal strain tensor ϵ_{ij} is symmetric and is given from the spatial gradients of particle displacement:

$$\epsilon_{ij} = \frac{1}{2}\left(\frac{\partial u_i}{\partial x_j} + \frac{\partial u_j}{\partial x_i}\right), \tag{1}$$

where u_i is the displacement along the ith unit vector direction, and x_i are the spatial coordinates see, for example, Aki and Richards (2009), chapter 2.1. Consequently, the temporal derivative of strain, or the strain rate, is

$$\frac{\partial}{\partial t}\epsilon_{ij} = \frac{1}{2}\frac{\partial}{\partial t}\left(\frac{\partial u_i}{\partial x_j} + \frac{\partial u_j}{\partial x_i}\right). \tag{2}$$

For a DAS cable elongated along the direction x_i, the system measures the (locally axial) strain ϵ_{ii}, or the associated strain rate:

$$\frac{\partial}{\partial t}\epsilon_{ii} = \frac{\partial}{\partial t}\frac{\partial u_i}{\partial x_i} = \frac{\partial}{\partial x_i}\frac{\partial u_i}{\partial t} = \frac{\partial}{\partial x_i}v_i, \tag{3}$$

where v_i is the particle velocity in the x_i direction. Similarly, by applying the chain rule to the equation above, the axial strain rate can be expressed in terms of axial acceleration and slowness components as (Baird et al., 2020; Daley et al., 2016)

$$\frac{\partial}{\partial t}\epsilon_{ii} = \frac{\partial}{\partial t}\frac{\partial u_i}{\partial t}\frac{\partial t}{\partial x_i} = a_i s_i, \tag{4}$$

where a_i is the acceleration and s_i the slowness in the x_i direction.

Hence, the DAS system allows for probing the particle velocity in the x_i direction by integrating over a finite cable length—the strain gauge length G. Likewise, the displacement can be extracted after integration in time.

For cable layouts that are not of a linear geometry, this sensitivity varies along the array of virtual sensors, as opposed to, for example, a conventional vertical-component array. We will show in this paper how to consider these effects when designing and processing DAS-arrays.

For P-waves in isotropic media, the particle motion is parallel to the wave propagation direction. The directional sensitivity of a DAS cable to particle motion and to P-waves is (Mateeva et al., 2014)

$$D_{\text{particle}}(\gamma_0) = \cos^2(\gamma_0), \tag{5}$$

where γ_0 is the local incidence angle of the impinging wave, relative to the cable axis. This sensitivity is hence zero for broadside arrivals ($\gamma_0 = 90°$). Conversely, the sensitivity is equal to one for particle motion along the cable axis. Note that Equation 5 is a linearized expression valid only for long enough wavelengths ($\gtrsim 4\times$) compared to the gauge length (Bóna et al., 2017).

For S-wave polarization, the associated particle motion is perpendicular to the wave propagation direction. The strain sensitivity depends on the angle of the cable axis from both the propagation vector and the polarization vector. If the propagation, polarization and cable axis vectors are all co-planar the angular dependence becomes

$$D_S(\gamma_0) = \sin(2\gamma_0). \tag{6}$$

Hence, this scaling factor can be negative, causing a polarity reversal when detecting S-waves.

Helically wound cables (HWC) offer a possibility to reduce this angular dependence. Kuvshinov (2016) provided the theoretical background for this approach, while Wuestefeld and Wilks (2019) demonstrated how this can be used for DAS acquisition design within microseismic applications. However, Baird (2020) demonstrated that HWCs are poorly suited for detecting S-waves as they reduce the sensitivity to S-waves for all propagation directions relative to straight fibers, while for tightly wound wrapping angles the apparent polarization will, in addition, completely reverse.

The analysis in the current paper focuses on the particle motion direction, making the interpretations most applicable for P-waves, but future generalizations can also account for the polarization effects required for interpreting S-waves.

2.1.2. DAS Gauge Length and the Highest Resolvable Frequency

In practical DAS signal processing, the time-series produced by the interrogator has been averaged over a time window, which corresponds to a spatial extent along the DAS cable: the gauge length. This averaging inherently results in a maximum temporal frequency (or minimum spatial wavelength) that the system can resolve. Moreover, the averaging introduces an additional directivity component in the sensitivity of the system, independent of the directivity of the cable sensitivity, as is further analyzed in Section 2.2.2.

For strain data to be acquired, there inherently needs to be a defined gauge length, that is, a spatial extent within the fiber over which deformation is determined. This gauge length is chosen in most systems prior to acquisition, and typical values for earth science applications are between 5 and 40 m, with 10 m being commonly used. Longer gauge lengths are more accurate in amplitude, but the signal is smoothed. An increase in gauge length typically increases the SNR in the measurements, while too long a gauge length will introduce additional directivity due to the effective spatial extent of the virtual array element given by the gauge length, hence reducing the amplitude of signals impinging from most directions.

With the possibility of setting the spacing Δx of (virtual) sensors along a fiber to be very dense, typically every 1 m or less, the gauge length is in effect a moving average, which can be seen as the spatial extent of a virtual array element, and which determines the spatial Nyquist frequency (Dean et al., 2017). Note that if the gauge length is reduced to smaller than the light pulse width, the relation between phase and strain becomes non-linear. Essentially, the strain sensed by a DAS system is thus the average strain over a section of fiber whose length

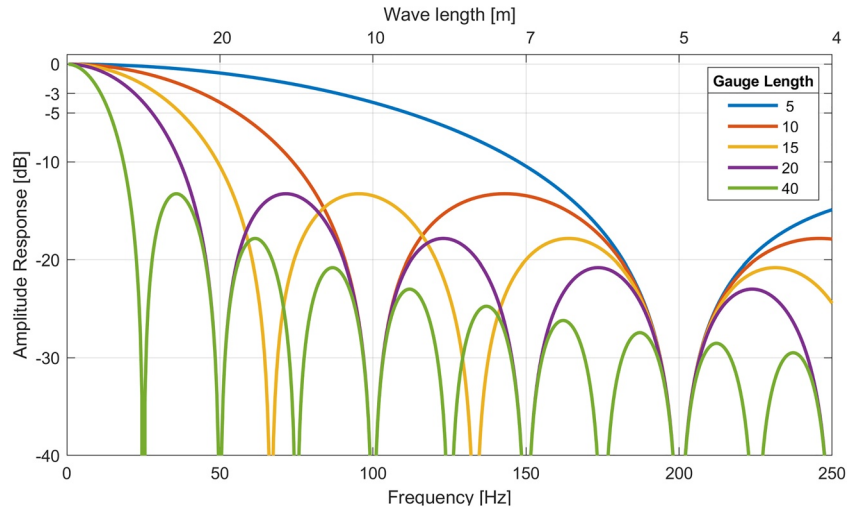

Figure 2. Amplitude response for several typical gauge lengths as a function of frequency (bottom x axis) and wavelength (top x axis).

is referred to as the gauge length, G. In the frequency domain, a moving average corresponds to a sinc-related function Smith (1997), Ch. 15:

$$R(\omega) = \frac{1}{N}\frac{\sin(\omega N/2)}{\sin(\omega/2)}, \tag{7}$$

where $N = G/\Delta x$ is the number of samples average, and $\omega = 2\pi(k\Delta x)$, with wavenumber k and spatial sampling interval Δx. Furthermore, substituting $k = 1/\lambda$, where λ is the wavelength, yields

$$R(\lambda) = \frac{\Delta x}{G}\frac{\sin(\pi G/\lambda)}{\sin(\pi \Delta x/\lambda)}. \tag{8}$$

The DAS cable response for a certain gauge length $R_{\text{gl}}(\lambda)$ can thus be determined (Dean & Correa, 2017) by:

$$R_{\text{gl}}(\lambda) = \frac{\Delta x}{G}\left|\frac{\sin(\pi G/\lambda)}{\sin(\pi \Delta x/\lambda)}\right| \tag{9}$$

In the regime of small arguments, $\sin(x) \approx x$ and the above can be approximated to

$$R_{\text{gl}}(\lambda) = \frac{1}{G}\left|\frac{\sin(\pi G/\lambda)}{\pi/\lambda}\right|. \tag{10}$$

Gauge averaging increases the SNR, and it can be shown (Dean et al., 2017) that the fiber strain SNR is maximized when the gauge length is

$$G_{\text{opt}} = \lambda/\sqrt{3}, \tag{11}$$

and in practical implementations the ratio G/λ is often between 0.4 and 0.54, selected based on a trade-off between SNR optimization, temporal resolution, and spatial resolution of the DAS system.

Figure 2 shows the response for a set of typical gauge lengths and a medium velocity of $V = 1{,}000$ m/s. As the DAS measurement is a result of a coherent summation of wave contributions along a section of fiber, destructive interference can occur, yielding a zero-amplitude strain estimate. Such notches in the response are inherent properties of moving average filters (Smith, 1997). These occur if the denominator in Equation 8 is zero, and thus at frequencies where the wavelength is an integer multiple of the gauge length:

$$k_{\text{notch}} = nG/\lambda, \quad n \in \mathbb{N}. \tag{12}$$

This relationship can guide the choice of gauge length prior to acquisition. Section S2 in Supporting Information S1 provides more background on the relation between wave velocity, gauge length, and the resolvable frequency.

2.2. Classical Array Signal Processing Concepts

In this section, we describe some basic concepts used in array processing, which are fundamental when considering the design and processing of DAS arrays. First, we introduce the method of beamforming and how a steered signal can help to identify coherent energy across an array. We then demonstrate how beamforming is related to the array response function, which can be used to optimize the design of an array as well as to understand its limitations. From these concepts, we incorporate the effects of directivity which are pertinent for DAS arrays. From the array response function, we describe how to estimate the array resolution and how to be aware of potential aliasing artifacts. We show how beam steering and power estimation as a function of horizontal slowness can be used to identify the direction and apparent velocity of the impinging wavefronts, before finally providing an explanation for SNR gain achieved from a sensor array.

2.2.1. Delay-and-Sum Beamforming and the Array Response Function

We assume that in an array of M sensors, each sensor, with spatial coordinates $\mathbf{r}$, records a time-series $y_m(t$; i.e., the seismic trace), which sample the physical wavefield $a(\mathbf{r}, t)$. In array signal processing, beamforming is a technique where a set of sensor traces are delayed, weighted, and stacked. See, for example, Johnson and Dudgeon (1992) for a general delay-and-sum concept description, or Schweitzer (2014); Rost and Thomas (2009) and the references therein for seismology-oriented introductions.

After applying a delay and a weight to each of the sensor traces, the summed (stacked) traces give the beamformer output, which is often simply denoted as the beam, which is:

$$z(t) = \frac{1}{M}\sum_{m=0}^{M-1} w_m y_m(t - \Delta_m), \tag{13}$$

where Δ_m are the applied time delays and w_m are the sensor weights (often denoted apodization weights, tapering, or shading) which in the simplest case are all set to one. The effect of applying non-uniform apodization weights is illustrated in Section S7 of Supporting Information S1.

In conventional delay-and-sum beamforming, the time-delays Δ_m are extracted from a pre-determined model, typically based on either a plane wave (far-field) or a spherical wavefront (near-field) assumption, see also Section S3 in Supporting Information S1 for explanations regarding the far-field limit.

Consider an ideal monochromatic (single-frequency) plane wavefield. Then the physical field that the sensors probe is $a(\mathbf{r}, t) = A_0 \exp\left(i\omega(t - \mathbf{s}_0 \cdot \mathbf{r})\right)$, where the wave has slowness $\mathbf{s}_0$, amplitude A_0, and angular frequency ω. Note that in the linear wave-propagation regime, any wavefield can be decomposed as a linear sum of such monochromatic plane waves using the Fourier transform. A time-delay applied to a monochromatic plane wave corresponds to a multiplication by a phase factor (a phase delay). Then, the delayed signal sensed by sensor m at location $\mathbf{r}_m$ becomes

$$y_m(t - \Delta_m) = e^{-i\omega\Delta_m} e^{i\omega(t - \mathbf{s}_0 \cdot \mathbf{r}_m)} = e^{i\omega(t - \Delta_m - \mathbf{s}_0 \cdot \mathbf{r}_m)}, \tag{14}$$

where for simplicity the amplitude is normalized to $A_0 = 1$. The beamformer output stack, Equation 13, can then be written as

$$z(t) = \frac{1}{M}\sum_{m=1}^{M} w_m e^{i\omega(t - \Delta_m - \mathbf{s}_0 \cdot \mathbf{r}_m)}. \tag{15}$$

In the array signal processing literature (e.g., Johnson & Dudgeon, 1992; van Trees, 2004), this beamformer output as well as its expected power, are often expressed using a steering-vector based formalism, as further outlined in Section S5 of Supporting Information S1.

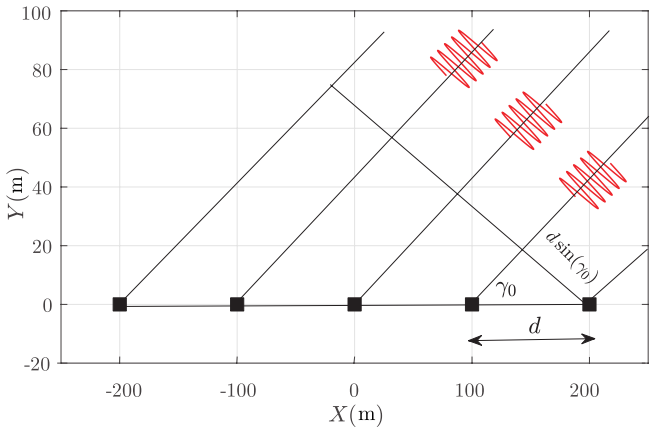

Figure 3. A uniform linear array with a sensor distance d and a wavefront impinging with the angle γ_0 from the cable axis.

The delays on each sensor trace can be freely set, and an obvious choice is to let $\Delta_m = -\mathbf{s}\cdot\mathrm{r}_m$ with the goal of stacking the sensor traces coherently (in phase), which corresponds to steering toward the impinging wavefront with slowness vector $\mathbf{s}$. Then the beamformer output stack becomes

$$\begin{aligned} z(t) &= \frac{1}{M}\sum_{m=1}^{M} w_m e^{i\omega(t+(\mathbf{s}-\mathbf{s}_0)\cdot\mathbf{r}_m)} \\ &= \frac{e^{i\omega t}}{M}\underbrace{\sum_{m=1}^{M} w_m e^{-i\omega(\mathbf{s}_0-\mathbf{s})\cdot\mathbf{r}_m}}_{\triangleq A(\omega,\mathbf{s}_0-\mathbf{s})}. \end{aligned} \tag{16}$$

This summation is a discrete spatial Fourier transform given by the sensor locations $\mathbf{r}_m$, the angular frequency ω, and a plane wave slowness. In the literature, $A(\omega\mathbf{s})$ is denoted with various terms such as the array response function, array transfer function, wavenumber-frequency response, or occasionally the array pattern. In the following, we use the term array response function.

The array response function is hence an inherent property given from the array geometry and it carries information about the frequency-dependent resolution characteristics as a function of angular frequency ω and slowness vector $\mathbf{s}$. The array response function is therefore often analyzed when designing and optimizing array geometries. As the slowness is related to the wave vector according to $\mathbf{k} = \omega\mathbf{s}$, the array response function can also be expressed in terms of $\mathbf{k}_0 - \mathbf{k}$:

$$A(\mathbf{k}-\mathbf{k}_0) = \frac{1}{M}\sum_{m=1}^{M} w_m e^{i\mathbf{r}_m\cdot(\mathbf{k}_0-\mathbf{k})}. \tag{17}$$

The array response function hence varies with frequency and additional sidelobes due to spatial aliasing can appear in the array response function if the inter-sensor spacing is greater than $\lambda/2$. For an optimized array response function, the amplitude of these side-lobes should be small compared to the main-lobe to reduce ambiguity effects in direction-of-arrival based analyses. This delay-and-sum signal processing can be seen as a spatial filtering which aims to reject signals from unwanted directions while keeping waves impinging from a given arrival direction (i.e., a given moveout signature characterized by the choice of Δ_m sensor trace delays).

Several key aspects of arrays are most straightforwardly illustrated by considering a uniform linear array (ULA) with uniform weights $w_m = 1$. Figure 3 displays a uniform linear array with sensor spacing d and a wavefront impinging at an angle γ_0. Using trigonometric identities and geometric series summation for an array of sensors located along the x axis separated by a uniform distance d, the array response function of an ULA is given by close-form expression (e.g., Johnson & Dudgeon, 1992, p. 117):

$$\begin{aligned} A(\mathbf{k}) &= \frac{1}{M}\sum_{m=1}^{M} e^{i\,d(m-M/2)\,k_x} \\ &= \frac{1}{M}e^{-i\,k_x M/2}\sum_{m=1}^{M} e^{id\,k_x\,m} = \frac{1}{M}\frac{\sin(k_x M d/2)}{\sin(k_x d/2)}. \end{aligned} \tag{18}$$

As a plane wavefront hits a ULA sensor m, it has traveled the additional length $md\sin(\gamma_0)$ compared to the distance traveled to the reference sensor. Hence, the beamforming procedure which applies the weights $\Delta_m = -\mathbf{s}\cdot\mathbf{r}_m = -md\sin(\gamma_0)$, seeks to compensate for this inter-sensor propagation time difference in order to align the signal traces in phase. When evaluating Equation 18 in terms of difference between the beam steering direction corresponding to $\mathbf{k}$—that is the direction corresponding to the moveout that the applied time-delays represent—and the wavenumber $\mathbf{k}_0$ of an incoming wave, we get

$$A(\mathbf{k}-\mathbf{k}_0) = \frac{1}{M}\frac{\sin\{(k_x-k_{x0})Md/2\}}{\sin\{(k_x-k_{x0})d/2\}}, \tag{19}$$

or equivalently in terms of direction-of-arrival γ_0 and steering direction γ

$$A(\theta, \gamma_0) = \frac{1}{M} \frac{\sin\{(\sin\gamma - \sin\gamma_0)\pi M d/\lambda\}}{\sin\{(\sin\gamma - \sin\gamma_0)\pi d/\lambda\}}, \tag{20}$$

where k_{x0} is the wavenumber component x of the impinging wave (coming from the angle γ_0) and k_x is the wavenumber component x toward which the beam is steered (angle γ).

In the classical delay-and-sum context, the array response function can be parameterized in terms of $\mathbf{s}_0 - \mathbf{s}$, which is the difference between the impinging wave slowness and the slowness corresponding to the applied steering delay moveout from Equation 16. Hence, for a given wave with slowness $\mathbf{s}_0$, the steered response pattern of a conventional array is the same, but translated, when evaluating over a $\mathbf{s}$ grid—the array response pattern is in this sense equivalent to the steered response (see, e.g., Johnson & Dudgeon, 1992, Section 4.2.3). However, in DAS systems the array elements have non-equal directional sensitivity and the corresponding steered response depends on $\mathbf{s}$ and $\mathbf{s}_0$. This is hence in general not equal to an array response parameterized in terms of $\mathbf{s} - \mathbf{s}_0$, as is further elaborated in Section 3.1.

2.2.2. Incorporating Sensor-Extent Related Directivity

For arrays where each sensor averages the wavefield over a certain spatial footprint, a directivity (which in the DAS case comes in addition to the fiber directivity of Equations 5 and 6) is introduced into the array response function (Johnson & Dudgeon, 1992; van Trees, 2004).

In the most general case, the inherent effect of averaging the wave over a physical element can be described using a spatial convolution integral to give the sensor signal

$$y_m(t - \Delta t) = \int_{-\infty}^{\infty} h_m(\chi) a(\mathbf{r} - \chi, t - \Delta t) d\chi, \tag{21}$$

where $h_m(\chi)$ is equal to one on the sensor m surface and zero otherwise. Hence, $h_m(\chi)$ is the physical extent over which the sensor is integrating the wavefield. Because a convolution corresponds to a multiplication in the frequency domain, for a unit amplitude monochromatic plane wave $a(\mathbf{r}, t) = \exp(i\omega(t - \mathbf{s}_0 \cdot \mathbf{r}))$ with wavenumber $\mathbf{k}_0 = \omega\mathbf{s}_0$, the spatial convolution in Equation 21 turns into a sum. This yields

$$y_m(t - \Delta t) = H_m(\mathbf{k}_0) e^{i\omega(t - \Delta_m - \mathbf{s}_0 \cdot \mathbf{r})}, \tag{22}$$

where $H_m(\mathbf{k}_0)$ is the spatial Fourier transform of the sensor extent $h_m(\chi)$. Note that $H_m(\mathbf{k}_0)$ remains the same also when time-delays are applied to the sensor trace. The beamformer output is then

$$z(t) = \frac{1}{M} \sum_{m=1}^{M} w_m H_m(\mathbf{s}_0) e^{i\omega(t - \Delta_m - \mathbf{s}_0 \cdot \mathbf{r}_m)}. \tag{23}$$

For the special case of identical element shapes and element directivities (which for the DAS case would correspond to identical gauge length and identical spatial orientation of each virtual element), $H_m(\mathbf{k}_0) = H(\mathbf{k}_0)$ for all m, the beamformer output can be simplified into

$$z(t) = \frac{H(\mathbf{k}_0)}{M} \sum_{m=1}^{M} w_m e^{i\omega(t - \Delta_m - \mathbf{s}_0 \cdot \mathbf{r}_m)}. \tag{24}$$

Therefore, the total array response function now has two factors: one based on the array pattern and one based on the spatial filter due to the element extent and the associated directivity:

$$A_{\text{tot}}(\mathbf{k} - \mathbf{k}_0) = H(\mathbf{k}_0) A(\mathbf{k} - \mathbf{k}_0). \tag{25}$$

We observe that for a straight DAS cable layout, Equation 25 can be applied to explain the directivity effect due to the gauge length averaging for array processing.

In array signal processing, the waves must be well-sampled in both space and time to avoid aliasing. To avoid the sidelobes (grating lobes) resulting from spatial aliasing, the array sensors have to sample the wavefield at intervals shorter than the spatial wavelength (see Sections S4 and S6 in Supporting Information S1 for further explanations of these well-established array signal processing concepts).

Aliasing hence occurs when the array is spatially undersampled, that is when the sensor spacing is too large compared to the wavelength. For DAS systems it is thus necessary to follow the Nyquist sampling theorem, and to avoid aliasing effects by selecting a sensor spacing which is equal to or less than half the shortest wavelength of the wave. See Section S4 in Supporting Information S1 for an illustration of spatial undersampling effects with a planar wave impinging a uniform linear array.

2.2.3. Resolution and Uncertainty From the Array Response Function

The size of a surface array, that is, its aperture, is the horizontal extent of the array. Because the array response function is a discrete spatial Fourier transform of the sensor layout (Equation 16), a wider aperture yields a narrower mainlobe as long as the signals are coherent at the sensors. The mainlobe width hence describes the array resolution, that is, its capability to resolve two nearby sources. Rost and Thomas (2009) list several rules of thumb regarding the array response function and the array resolution.

The mainlobe width is often measured at −3 dB compared to the maximum (the full-width at half maximum point) and describes the array resolution. For a uniform linear array with the aperture width D, the −3 dB limit is approximately at $0.89\lambda/D$. For a linear array with the sensor spacing $d = \lambda/2$, this corresponds to an azimuthal mainlobe width (or opening angle) of $\Delta\gamma_{3dB} = 2/N$.

Another parameter to consider is the contrast resolution of the system: This is determined by the array response sidelobe structure. Larger sidelobes reduce the SNR in the presence of omnidirectional noise, or when competing sources arrive at a horizontal slowness coinciding with a sidelobe. The sidelobe level can be characterized by for example, its maximum value or the average level outside of the mainlobe. The sidelobe level describes the array performance in terms of SNR and artifacts due to aliasing.

In DAS systems, the spatial sampling rate can be set very densely compared to the case of conventional seismic arrays. As further analyzed in Section 2.2.5, this DAS capability can be a great advantage when suppressing incoherent noise in the signal stack. Still, it may be decided in the processing to down-sample the data due to limitations in data storage. We emphasize here that aliasing effects should be considered in deciding the down-sampling for DAS array acquisitions.

2.2.4. Signal Power Estimate in Slowness Space, Steered Response and *f–k* Analysis

For a horizontal-planar array, the beam steering can be seen as an s_x and s_y projection of $\mathbf{s}$, where each (s_x, s_y) coordinate corresponds to a steering direction. It can be convenient to interpret the horizontal slowness in terms of backazimuth ϕ and apparent velocity v_{app}. The incidence angle θ and horizontal slowness have the following relation:

$$|\mathbf{s}_{\text{horizontal}}| = \frac{\sin\theta}{v_c}, \tag{26}$$

where v_c is the wave velocity.

The apparent velocity, also denoted trace velocity or ground speed, is the inverse of the horizontal slowness: $v_{\text{app}} = 1/|\mathbf{s}_{\text{horizontal}}|$. The backazimuth ϕ is the horizontal direction-of-arrival measured clockwise from the north, is given from the relation

$$\tan\phi = \frac{s_x}{s_y}. \tag{27}$$

Hence, using Equations 26 and 27 and the inverse trigonometric functions, we can map from (s_x, s_y) to incidence angle θ and backazimuth angle ϕ.

See Section S9 in Supporting Information S1 for a synthetic illustration of the steered response as a function of horizontal slowness on the NORES array. The inverse length of the vector $1/\sqrt{s_x^2 + s_y^2}$ from the origin of the slowness space to the maximum power and depicted in red is equal to the apparent velocity. The angle $\arctan(s_y/s_x)$ is the backazimuth estimate for the dominating wavefront in the analyzed data time window. The (s_x, s_y) location of maximum power maps to the wave parameters of the dominating wavefront, as illustrated in Section S9 of Supporting Information S1 also for real recordings of a regional earthquake recorded at NORES. The phase arrival times together with estimated backazimuth and apparent velocity can then be used to locate the epicenter of the

earthquake. Such array-derived parameters are exploited routinely by earthquake analysis centers worldwide and also in more detailed regional research studies (e.g., Jerkins et al., 2020), and are also becoming used in microseismic monitoring (e.g., Oye et al., 2021). For large DAS layouts the processing can be made over sub-arrays which each provide a direction-of-arrival and precise onset time which can be piped into seismic event location algorithms together with readings from other arrays, 3-component stations, or single-component stations.

2.2.5. White Noise Array-Gain

The array signal processing is able to filter out directional waves that interfere (or "jam") the wave of interest and the array response function can be regarded as a spatial filter which illustrates to what extent plane waves with a given wavenumber $\mathbf{k}$ can be resolved. In addition, by adding signals coherently and spatially white noise incoherently, the array signal processing can increase the SNR (see, e.g., van Trees, 2004, Section 2.6, or Johnson & Dudgeon, 1992, Section 4.5). This theoretical increase in SNR resulting from the array signal stacking is determined by the number of sensors deployed in the array as well as by the extent to which the signal traces are coherent between the sensors compared to the spatial coherence of the noise field. Following the derivation in Section S8 of Supporting Information S1, the array gain, AG, which is the SNR for the array divided by the SNR for a single sensor in terms of expected power becomes:

$$\mathrm{AG} \triangleq \frac{\mathrm{SNR}_{\mathrm{array}}}{\mathrm{SNR}_{\mathrm{sensor}}} = \frac{\left|\sum_{m=1}^{M} w_m\right|^2}{\sum_{m=1}^{M} |w_m|^2}. \tag{28}$$

For uniform weights $w_m = 1$, the array gain becomes $M^2/M = M$ independent of the element positions, as long as the noise is uncorrelated between the sensor traces. Our analysis in the following section will show that the directional sensitivity of DAS can be mapped into a non-uniform w_m weight framework. The array signal processing hence increases the SNR in terms of power by a factor M, which corresponds to a factor $\sqrt{M}$ in terms of signal amplitude. In circumstances where the spatial correlation length of the noise, the capability of DAS to sample the wavefield with a large number of virtual sensors, can hence be a great advantage in terms of white-nose gain, compared to conventional arrays with a smaller number of sensors.

3. Methods Developed

3.1. Adapting the Array Signal Processing Framework to a DAS Context

We now seek to incorporate the effects of DAS cable directivity and gauge length averaging into the array signal processing framework. This will lead to equations that explain the steered response of a DAS array. As we will show, these are straightforward to implement numerically.

Recognizing that the cable directional sensitivity of a DAS system can be regarded as a direction-dependent amplitude weight on the particle motion recorded by each virtual sensor, we generalize the beamformer output expression Equation 13 to not only include the user-selected apodization weights w_m (see Section 2.2), but also an additional DAS cable directivity weight $q_m(\mathbf{s}_0)$ on each sensor. Note that when the full channel data is accessible in the processing chain, the apodization weights w_m can, just like the sensor trace time-delays Δ_m be varied freely by the processing pipeline algorithm (each trace can freely both be multiplied by a constant and shifted by a chosen delay before all traces are stacked). This is exploited in several adaptive beamforming algorithms where also the spatial structure of the recorded wavefield is taken into account instead of (or in addition to) using a pre-defined plane-wave or spherical-wave model for the time delays and a pre-selected apodization function for the weights w_m. In the most straightforward setting the weights are uniform and $w_m = 1$ for all m.

The additional sensor amplitude weight $q_m(\mathbf{s}_0, \mathbf{r})$ is hence due to the intrinsic physical directivity in sensitivity to particle motion of each DAS virtual sensor which depends on the local direction-of-arrival in relation to the broadside of the cable elongation (cf., Section 2.1.1. This is the sensitivity $D_{\mathrm{particle}}(\gamma_0)$ of Equation 5), which in this DAS cable directivity context gives

$$q(\mathbf{s}_0, \mathbf{r}) = \cos^2(\gamma_0), \tag{29}$$

where $\gamma_0 = \text{atan}\,(\gamma_i(\mathbf{r}) - \gamma_s(\mathbf{s}))$ denotes the angle between broadside of the virtual DAS sensor and the particle motion associated with the impinging wavefront and for P waves in isotropic media, the particle motion is along the direction of propagation. Here, $\gamma_i(\mathbf{r})$ is the local direction of the DAS cable elongation, and $\gamma_s(\mathbf{s}) = \text{atan}(s_x/s_y)$. The virtual sensor weight q is hence a function of horizontal slowness and the local cable orientation, which in turn can vary with the spatial coordinate $\mathbf{r}$.

Taking the user-selected weights w_m, the direction-dependent sensitivity $q(\mathbf{s}_0, \mathbf{r})$, and the spatial wave integration over the virtual gauge-length element extent $h_m(\mathbf{r})$ (see Equation 21), the time-domain beamformer output becomes

$$z(t) = \frac{1}{M}\sum_{m=0}^{M-1} w_m \int_{-\infty}^{\infty} h_m(\mathbf{r})\, q(\mathbf{s}_0, \mathbf{r}) a(\mathbf{r}, t - \Delta_m) d\mathbf{r}, \tag{30}$$

where the spatial function $h_m(\mathbf{r})$ is equal to one for all sensor points covered by the gauge length of virtual sensor m, and zero otherwise.

For a sufficiently short gauge length, it can be reasonable to assume that the travel-time difference due to the shape curvature over the virtual element is negligible compared to the planar wavefront and the associated phase-shift. For cases when this approximation is appropriate, the direction-dependent weights can be assumed to be constant over each element and depend only on the center position of the virtual element. Then, the beamformer output (30) can be simplified to

$$z(t) = \frac{1}{M}\sum_{m=0}^{M-1} w_m q_m(\mathbf{s}_0) \int_{-\infty}^{\infty} h_m(\mathbf{r})\, a(\mathbf{r}, t - \Delta_m) d\mathbf{r}, \tag{31}$$

where $q_m(\mathbf{s}_0)$ is the amplitude weight due to cable directivity of virtual element m given a wave with horizontal slowness $\mathbf{s}_0$. For a monochromatic plane wave, we hence get a generalized delay-and-sum beamformer output:

$$z(t) = \frac{1}{M}\sum_{m=1}^{M} w_m q_m(\mathbf{s}_0) H_m(\mathbf{k}_0)\, e^{i\omega(t - \Delta_m - \mathbf{s}_0 \cdot \mathbf{r}_m)}, \tag{32}$$

where $H_m(\mathbf{k}_0)$ is the spatial Fourier transform of $h_m(\mathbf{r})$, akin to the factor in Equation 23 for array processing with conventional directional elements. In the DAS context, the spatial extent of this integral over each virtual element is hence decided by the gauge length setting.

For the standard choice of focusing delay to align the sensor traces, $\Delta_m = -\mathbf{s} \cdot \mathbf{r}_m$, we get

$$z(t) = \frac{e^{\omega t}}{M}\sum_{m=1}^{M} w_m q_m(\mathbf{s}_0) H_m(\mathbf{s}_0)\, e^{-i\omega(\mathbf{s}_0 - \mathbf{s}) \cdot \mathbf{r}_m}. \tag{33}$$

In Equation 33, we see that it is not possible to parameterize the expression in terms of $\mathbf{s} - \mathbf{s}_0$, as is the definition of the array response function (Equation 16). Instead, (33) has to be re-evaluated for each impinging wave direction $\mathbf{s}_0$ and the *steered response* for a given $\mathbf{s}_0$ is found by sweeping $\mathbf{s}$ and calculating the beamformer output for each relevant (s_x, s_y) value. Hence, in order to get a comprehensive understanding of the array's capabilities, we have to evaluate the steered response for all relevant $\mathbf{s}_0$.

We note that, since the weights w_m can be freely selected, for each sensor element these are possible to adjust to compensate for the q_m factor. Independent from the current work, the conference presentation Bowden et al. (2021) presents an approach which essentially is similar to balancing w_m so that $w_m q_m = 1$.

A straightforward approach would hence be to let $w_m = 1/q_m$ based on the slowness $\mathbf{s}$ of the beam steering: $w_m = w_m(\mathbf{s})$. However, this method would break down whenever $q_m = 0$, so it could be advised to instead apply some stabilized manner which does not blow up the amplitude of w_m to infinity. For example, w_m could be set to zero in order to disregard all virtual elements which are insensitive to the slowness $\mathbf{s}_0$.

3.2. Numerical Workflow to Estimate the Full DAS System Steered Response

To assess the array processing capabilities of an existing or planned array given an impinging wavefront with horizontal slowness vector $\mathbf{s}_0$, we seek to estimate Equation 30 numerically.

Hence, in order to estimate the consolidated directional sensitivity (the steered response for multiple directions) of a DAS system for waves impinging from the far-field at a given horizontal slowness (s_{x0}, s_{y0}), the gauge length G, the geometrical layout, the virtual sensor separation d, and the wave frequency f need to be taken into account. We assume a locally homogeneous medium with phase velocity V.

A numerical estimate of Equation 30 can be achieved by discretization of the DAS layout into N closely-spaced, equidistant sampling points, with K points distributed on each virtual sensor. We denote the sampling element with indices corresponding to sensor m as $k_{m1}, \ldots, k_{mK}$. Hence, $N = M \cdot K$ and the beamformer output is estimated, using a numerical average over the virtual elements instead of an integral, numerically as

$$z(t) = \frac{1}{MK} \sum_{m=0}^{M-1} w_m \sum_{k=1}^{K} q(\mathbf{s}_0, \mathbf{r}_{mk})\, a(\mathbf{r}_{mk}, t - \Delta_m), \tag{34}$$

where $\mathbf{r}_{mk}$ is the location of sampling element k of virtual element m. The following numerical workflow based on Equation 34 can hence be used to estimate the DAS system steered response as a function of steering slowness $\mathbf{s}$ to a wave slowness $\mathbf{s}_0$. First, synthetic data traces are generated:

1. A set of K closely spaced sampling points are distributed along the cable. These are equidistant and separated less than half the wavelength
2. A synthetic time-signal $a'(t')$ is generated for a time axis starting at $t' = 0$, sampled well below the temporal Nyquist frequency. In the current study, we employ a single-frequency sinusoid. Still, the method allows for using other wave models, for example, extracted from data recordings, empirically modeled wavetrains, or idealized pulses like Ricker wavelets.
3. Given the slowness $\mathbf{s}_0$ of the impinging wave under consideration, the relative propagation time τ_{mk} is calculated for all K sampling points. This relative propagation time can also be estimated for more complex velocity distributions as long as models for the relative time-delays between the sensors can be found.
   Then follow the beamforming-related steps:
4. Given the analyzed steering slowness $\mathbf{s}$, and the location $\mathbf{r}_{mk}$ of each virtual element we apply the plane-wave steering delays $\Delta_m = -\mathbf{s} \cdot \mathbf{r}_m$, to the K sampling points of virtual sensor m, located within one gauge length.
5. Shifting the time-signal $a(\mathbf{r}_{mk}, t)$ given in (2) by the delay τ_k given in (3) yields the following model for the delayed signal trace at the location $\mathbf{r}_{mk}$:

$$a(\mathbf{r}_{mk}, t - \Delta_m) = a'(t' - \tau_{mk} + \mathbf{s}_0 \cdot \mathbf{r}_m). \tag{35}$$

6. Then, the time-shifted synthetic signals are stacked: first over each set of K sample elements and then over each virtual element m:

$$z'(t) = \frac{1}{MK} \sum_{m=0}^{M-1} w_m \sum_{k=1}^{K} q(\mathbf{s}_0, \mathbf{r}_{mk})\, a'(t' - \tau_{mk} + \mathbf{s}_0 \cdot \mathbf{r}_m), \tag{36}$$

   We apply the weights $w_m = 1$, but underline that other apodization, or directivity-compensating weights can be applied.
7. Finally, the beamformer output power corresponding to $\mathbf{s}$ is found as the temporal average of $|z'(t)|^2$.

This workflow is applied for all steering horizontal slowness points of interest $\mathbf{s}$ to yield an estimate of the steered response, which is applied in the case studies and analyses following in Section 4.

We note that these estimates may also be found from the frequency-domain variant Equation 33 for cases when the template waveform approximates a continuous single-frequency (monochromatic) sinusoid and the gauge length is short enough to have the same directional sensitivity over each virtual element.

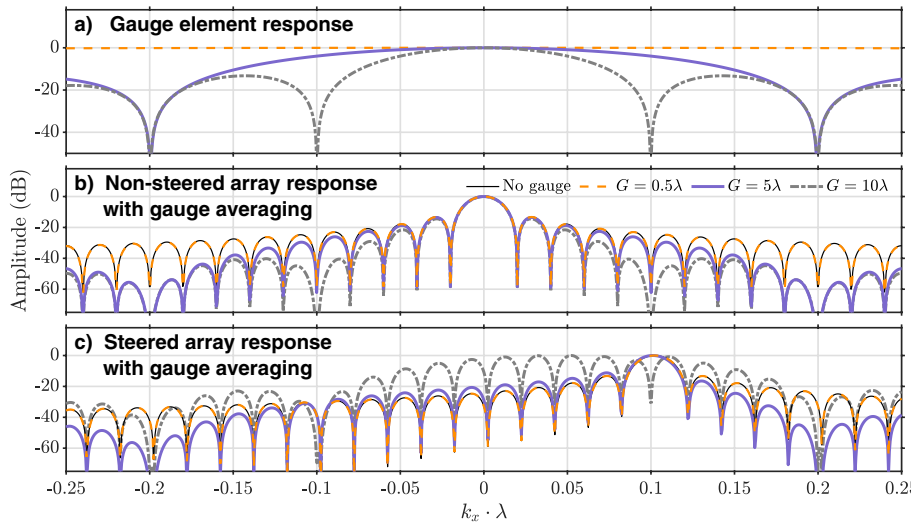

Figure 4. The effect of gauge length averaging on the response of a uniform linear array, evaluated as a function of normalized x component of the wavenumber. Examples are given for the gauge lengths 0, 0.5λ, 5λ, 10λ. The cable directivity is neglected. (a) the directional effect due to the different gauge-lengths for $G = 0.5\lambda$ (red dashed line), $G = 5\lambda$ (solid purple line), and $G = 10\lambda$ (dash-dotted gray line). (b) The array steered responses when the wavefronts are parallel to the DAS axis. (c) The array steered responses when the wavefronts are impinging with $k_x = 0.1/\lambda$. All responses are normalized to their respective individual maximum.

The methods developed highlight that in DAS array performance analysis, the steered response for the set of direction-of-arrival of interest for a particular design has to be taken into account. The steered response is a function of both $\mathbf{s}$ and $\mathbf{s}_0$, but cannot in general be parameterized in terms of the difference $\mathbf{s} - \mathbf{s}_0$ like the conventional array response function.

4. Results

4.1. Illuminating Gauge Length Effects Using a Linear Layout Example

A key question when applying array signal processing recipes to DAS data is: how long can the gauge length be without degenerating the array resolution? To illustrate gauge length influence on the array directivity, here we assess steered responses for a linear DAS layout of length 40λ for a set of gauge lengths between $G = 0.5\lambda$ and $G = 10\lambda$. For simplicity, this analysis disregards the effect of the cable directivity, which is equivalent to setting $q(\mathbf{s}_0, \mathbf{r}_{mk}) = 1$ in Equation 36. Hence, for this case with equidistant virtual elements, of the equal size and orientation, the effects due to gauge-length averaging can be modeled using Equation 25. The size of the virtual element spanned by the gauge length is then associated with a response directly related to the element directivity. Following Equation 24, this can then be multiplied by the steered array response of a set of conventional sensors located at the same sites as the center of each DAS virtual element to generate the total steered response.

Figure 4 displays the total response when varying the gauge length both for an impinging wavefront parallel to the cable axis and for a wavefront with $k_x = 0.1/\lambda$. The greater the gauge length, the narrower is this element response (Figure 4, top panel). The analysis in this figure confirms that for $G \leq \lambda/2$, the gauge-length averaging causes negligible directional distortion (top panel, the flat orange dashed line) on the total response. This is valid for wavefronts parallel as well as for wavefronts which are not parallel to the cable axis.

For wavefronts parallel to the cable axis, we also note that even for large gauge lengths, for example, $G = 10\lambda$, the effects on the main lobe and the first sidelobes is small or negligible. On the contrary, for wavefronts not parallel to the cable axis, the gauge element response cannot be adjusted by applying beam steering delays and hence always has its mainlobe toward $k_x = 0$. Hence, the element responses affect the total steered response significantly – typically to a greater extent for greater k_x of the impinging wave. In the bottom panel of Figure 4, the steered response (with gauge length effects included) features a mainlobe relative unaffected at $G = 5\lambda$. But as G increases, the first zero in the element response approaches the steering k_x, and for $G = 10\lambda$ there is a null in

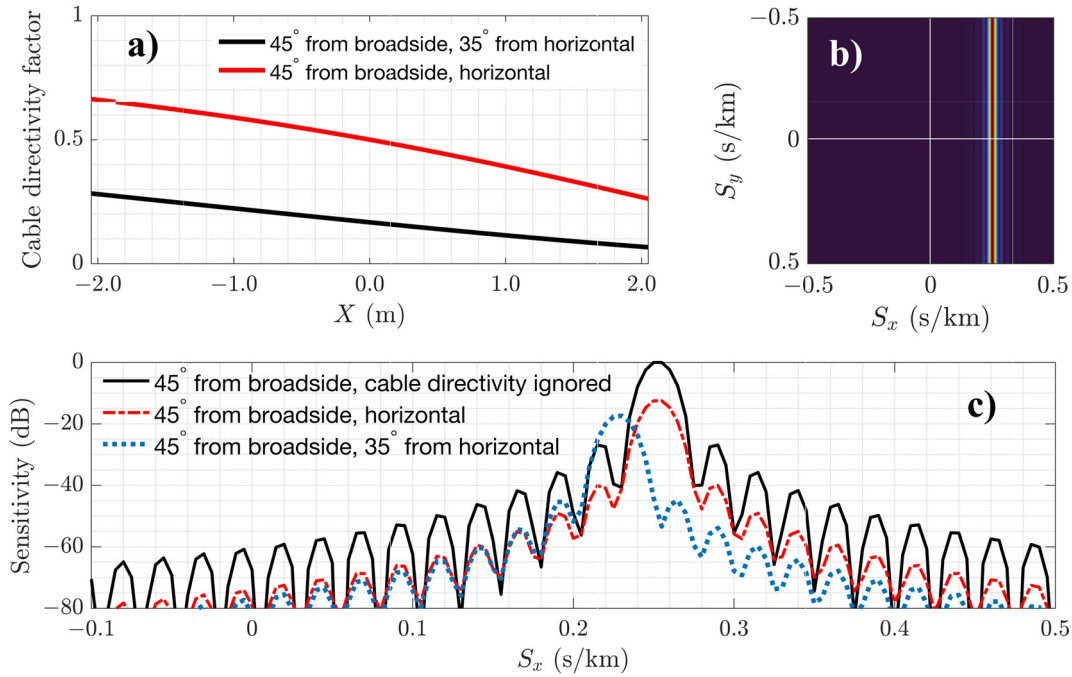

Figure 5. Linear DAS fiber array response to P-wave with frequency 10 Hz crossing the cable at 45° from broadside in a medium with 4,000 m/s P-phase velocity. The cable aperture is 4 km, spanning a straight line between $x = -2$ km and $x = 2$ km. (a) Sensitivity due to the cable directivity for each sensor to a wave impinging at 45° from broadside, either horizontally or at 35° from vertical. (b) steered response to the same wave as a function of horizontal slowness. (c) S_x component of the steered response to a wavefront moving horizontally (red) and at an angle of of 35° from broadside (blue). The steered response when the cable directivity is neglected is shown in black.

the element response at $k_x = 0.1/\lambda$, which even splits the total steered response mainlobe to severely degrade the beamforming performance.

For DAS layouts that are not linear, the spatial Fourier transform of each virtual gauge-length element is not uniform and the simplifications of Equations 24 and 25 are not valid. Instead, the total effect of gauge length-induced directivity, array layout steered response, and cable directivity have to be evaluated separately for each impinging wavefront slowness $\mathbf{s}_0$ as given by Equation 33. A take-away message of the gauge length analysis in the current section is that for $G \leq \lambda/2$, there are no additional steered response directivity effects due to gauge length averaging to be expected for any direction of arrival. This G criterion is more relaxed than the $G \leq \lambda/4$ limit for which the cable directivity can be written as $D_{\text{particle}}(\gamma_0) = \cos^2(\gamma_0)$ (see Section 2.1.1 and Equation 5), but we note that including additional terms in the Taylor expansion of the exponentials in Bóna et al. (2017, Equation 7) can allow for a refined $D_{\text{particle}}(\gamma_0)$ expression.

4.2. Comparing Fundamental DAS Deployment Layouts

Expanding the analysis of linear DAS array steered response using Section 3.2 framework, we explore how this depends on the incidence angle of a plane wave impinging at 45° backazimuth. Figure 5 compares the steered response when the cable directivity is neglected to cases when the cable directivity is taken into account and the incidence angle is varied. This confirms that a linear east–west layout provides no resolution in the s_y slowness direction.

Figures 6, 7, and 8, analyze steered responses calculated for L-shaped, triangular, and spiral DAS layouts with wavefronts impinging from three different backazimuth directions, with and without taking the cable directivity into account.

The L-shape geometry (Figure 6) naturally features a significant angular dependence in the response. Notably, when the cable directivity is taken into account, the steered response features this for waves arriving parallel

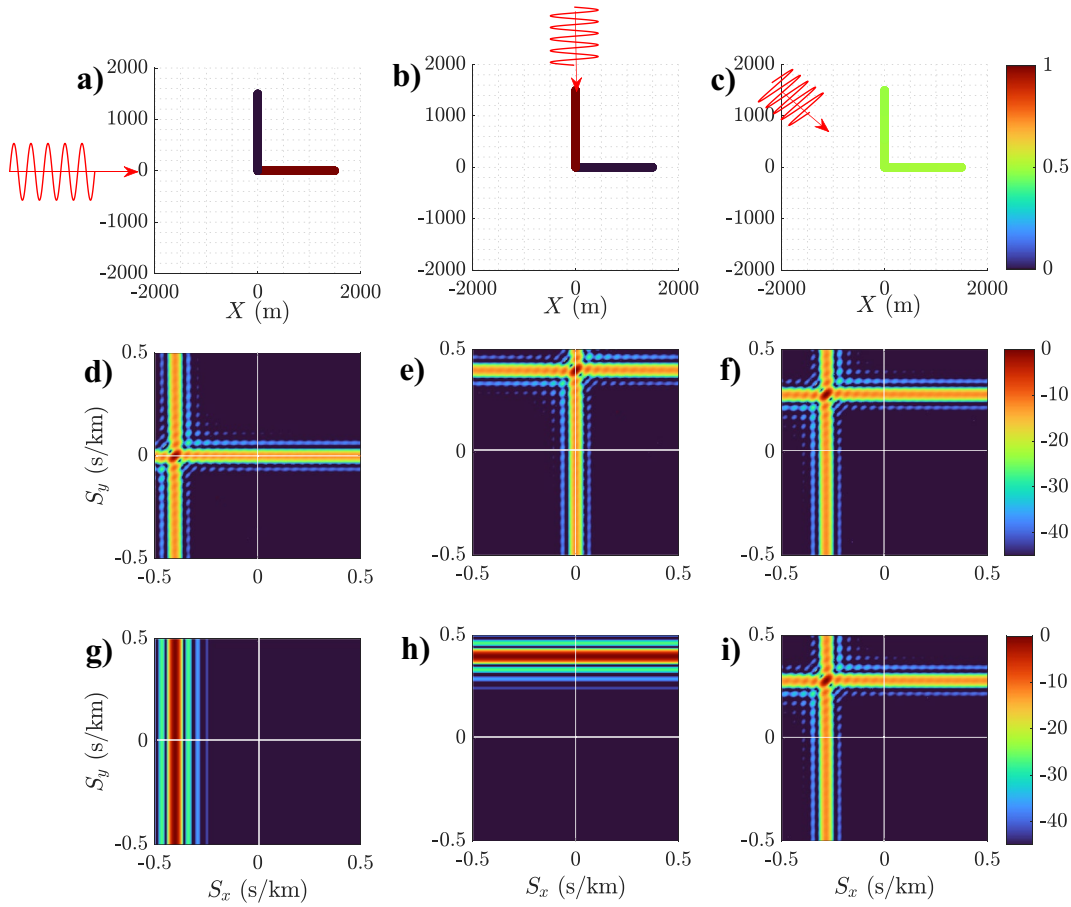

Figure 6. Steered responses to impinging P-waves, calculated for an L-shaped DAS geometry for $V = 2.5$ km/s and $f = 20$ Hz., corresponding to $|k| = f/V = 0.008$ m^{-1}. Top row: the directional sensitivity for each cable virtual sensor when the wavefront impinges from (a) west with $(k_{x0}, k_{y0}) = (-0.008, 0)$ m^{-1}, (b) north with $(k_{x0}, k_{y0}) = (0, 0.008)$ m^{-1}, and (c) northwest with $(k_{x0}, k_{y0}) = (-0.0057, 0.0057)$ m^{-1}. Middle row, (d), (e), and (f) Steered response for waves from the same three directions, calculated without taking the cable directivity into account. Bottom row, (g), (h), and (i) Steered response for waves from the same three directions, calculated with the cable directivity taken into account.

to an axis of the DAS cable. Triangle shaped layouts (Figure 7, e.g., Hudson et al., 2021), are hence expected generate a more homogeneous response if all backazimuth directions are of equal interest. Both the L-shaped and the triangular arrays can still be well-suited for missions where a homogeneous steered response is of less importance. Spiral-shaped layouts like in Figure 8 feature cable segment axes distributed in all directions and thus give a more homogeneous steered response as function of backazimuth. Note that by varying the number of loops, loop radius, and spacing the steered responses can be tuned. However, this geometry also results in greater cable elongation which would be associated with increased costs.

4.3. Steered Response for the NORES Array Experimental DAS Deployment

The NORES regional seismic array in southern Norway currently has 16 3-component broadband sites distributed over an aperture of around 1.4 km with its central sensor site at 60.7353°N, 11.5414°E (Kværna, 1989; Schweitzer et al., 2021). Although not explicitly a part of the International Monitoring System (IMS) for the Comprehensive Nuclear-Test-Ban Treaty, this array partly overlaps with the large-aperture IMS primary seismic array NOA (Dahlman et al., 2011). Nine stations in the NORES array are also equipped with microbarometers designed to register atmospheric infrasound (Gibbons, Asming, et al., 2015; Gibbons, Kværna, & Mykkeltveit, 2015). The site also features a 9-arm optical cable network that connect the central site to the array elements, including an additional 9 array elements in the 'D-ring' which are no longer operational (Figure 1). This established infrastructure makes the NORES site an excellent laboratory for validation and assessment of DAS array

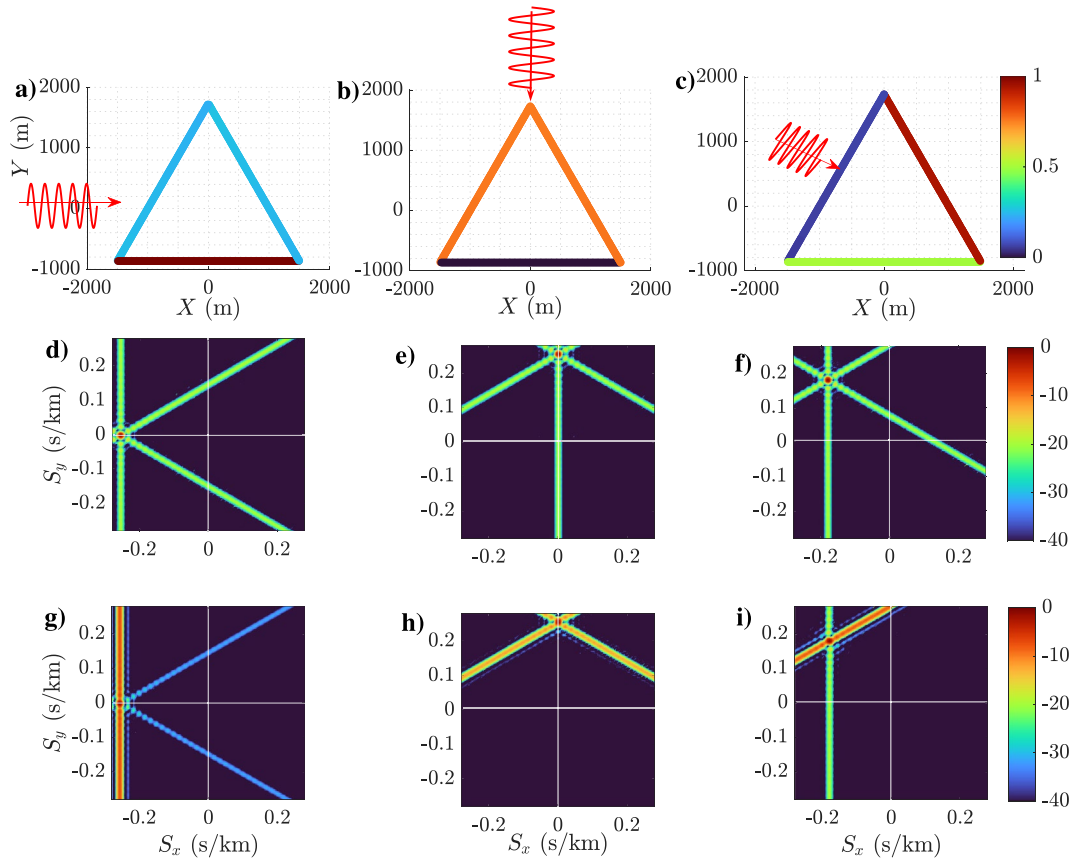

Figure 7. Steered responses to impinging P-waves, calculated for a triangular DAS layout for $V = 3.5$ km/s and $f = 20$ Hz, corresponding to $|k| = f/V = 0.0057$ m^{-1}. Top row: the directional sensitivity for each cable virtual sensor when the wavefront impinges from (a) west, (b) north, and (c) northwest. Middle row, (d), (e), and (f) Steered response for waves from the three different directions, calculated without taking the cable directivity into account. Bottom row, (g), (h), and (i) Steered responses calculated with the cable directivity taken into account.

measurements. Figure 9 shows the steered response for each NORES DAS arm individually, with and without taking the cable directivity into account, for a wavefront crossing at 315° with high apparent velocity. The respective combined responses of the full fiber layout are then displayed in the bottom row. We note that, given this direction of arrival, the steered response of individual arms can differ significantly when the cable directivity is taken into account (arms 2, 5, 6, 8). Still, the steered response of the full layout features similar main lobe width and sidelobe shapes of similar amplitude with and without taking the cable directivity into account.

5. Discussion and Conclusions

This study has analyzed DAS array signal processing, in particular highlighting the importance in DAS analysis to take the *steered response* array signal processing concept into account — in contrast with the more general *array response function* concept valid for conventional arrays. A key underlying aspect is that the DAS cable is blind to broadside particle motion but has maximum sensitivity along the cable axis is taken into account. For cable layouts that are not linear in shape, this directivity varies between the virtual DAS sensors. The gauge-length averaging can also introduce spatial wavefield filtering effects. Our analysis based on the incorporation of element responses into array signal processing theory highlights that as long as the gauge length is below half the wavelength, gauge length averaging effects are not expected to degrade the array steered response.

Employing concepts from well-established array signal processing theory we have developed equations and a numerical framework to estimate the steered response to particle motion of seismic wave arrivals on DAS arrays: For each given impinging wave slowness, our methodology maps the DAS cable layout, the gauge length, and the

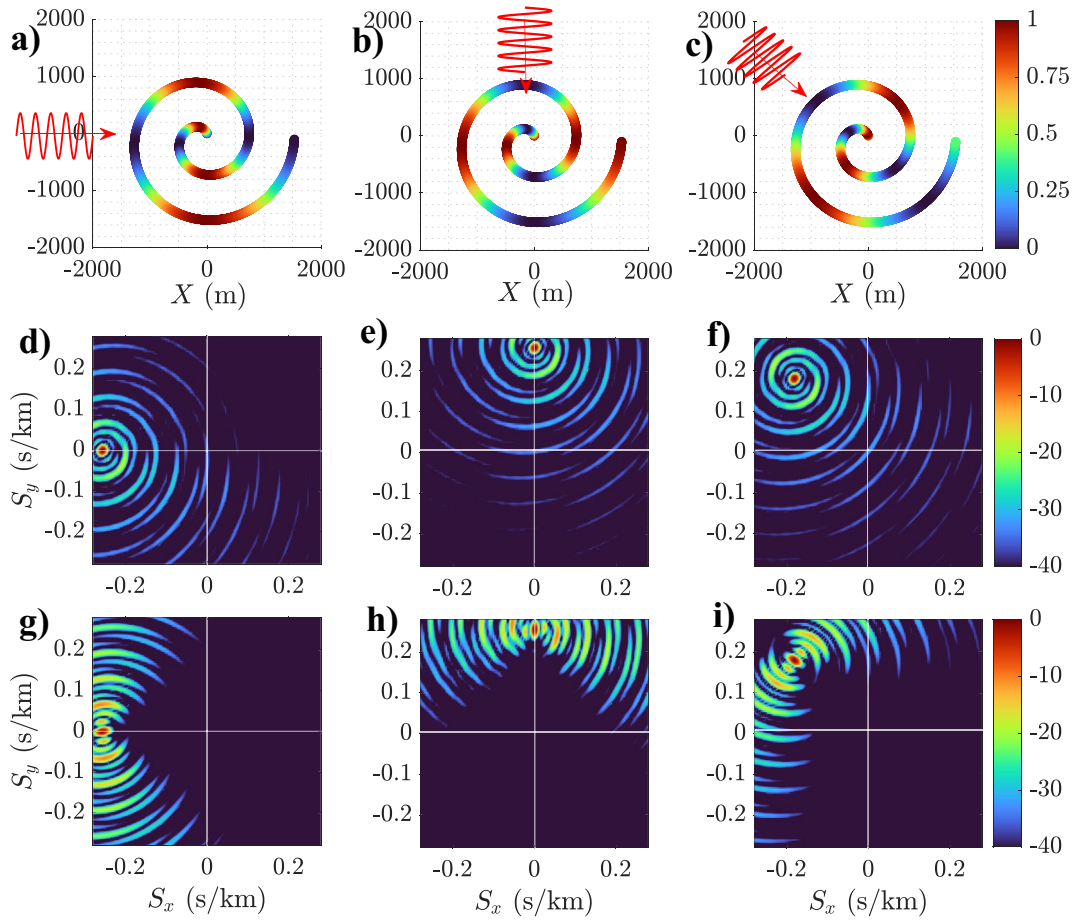

Figure 8. Steered responses calculated for a spiral shaped DAS fiber layout for $V = 3.5$ km/s and $f = 20$ Hz, corresponding to $|k| = f/V = 0.0057$ 1/m and P-waves impinging from three different directions. Top row: the directional sensitivity for each cable virtual sensor when the wavefront impinges from (a) west, (b) north, and (c) northwest. Middle row, (d), (e), and (f) Steered response for waves from the three different directions, calculated without taking the cable directivity into account. Bottom row, (g), (h), and (i) Steered responses calculated with the cable directivity taken into account.

cable directivity effects into the framework of steered response. Effects due to a finite gauge length are handled in the same manner as directional sensors of finite spatial extent are taken into account in classical array signal processing. Spatial filtering due to the directional sensitivity of the cable are taken into account as virtual sensor weights in a similar manner as sensor apodization (aperture shading or tapering) is incorporated in array signal processing theory.

DAS layout design principles and spatial filtering capability estimation frameworks have previously not been established in a similar manner as for conventional seismic arrays. Our finding that we cannot form an array response function like is done for conventional arrays but that instead the steered response has to be analyzed for the directions of arrival of interest (the horizontal slowness regime) of the relevant DAS array monitoring missions, is an important aspect when developing DAS array layout design principles. Another aspect is that the very nature of the DAS technology requires a continuous cable line, while still connecting segments or even return loops in the same cable might be considered.

We note that our theoretical framework of Section 3.1 confirms the findings of Bowden et al. (2021) that cable directivity effects can to some extent be compensated for when the curvature over each gauge length is short enough compared to the seismic signal wavelength. On the other hand, neither van den Ende and Ampuero (2021) nor Nayak et al. (2021) take into account all direction-dependent sensitivity aspects discussed in the current paper. Future extensions of these works might hence benefit from the frameworks presented.

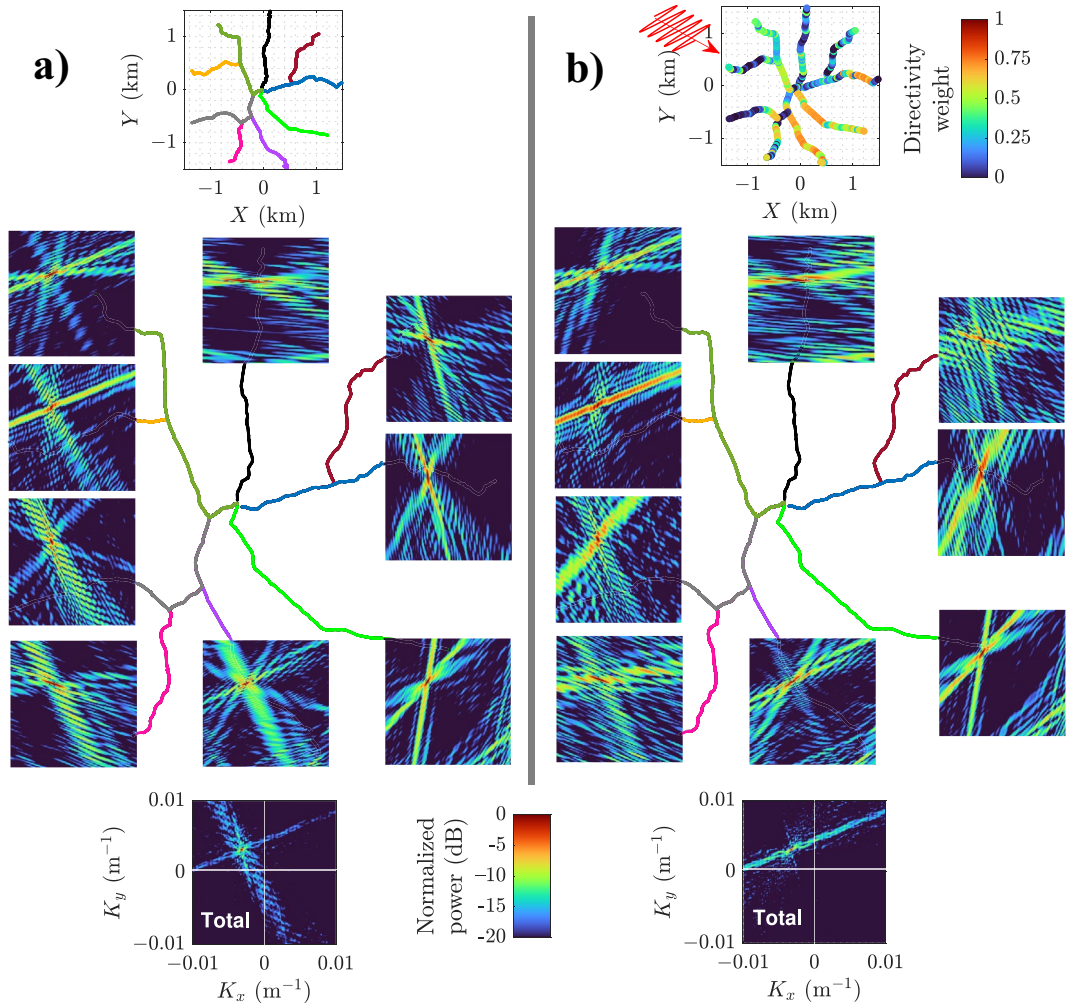

Figure 9. NORES DAS deployment steered response to a wave impinging from 315° backazimuth, evaluated for each of the 9 cable arms of the array. Left panels (a): the steered response for each individual arm and for the full array as it would have appeared without taking the cable directivity into account. The individual arm response plots are positioned corresponding to the different DAS array arm locations, for which the layout is shown in the background. The total response is displayed in the bottom panel. Right panels (b): the steered response for each individual arm and for the full array when also taking the cable directivity into account.

An interesting opportunity in the extended wavefield sampling opportunities provided by the prospects of using closely spaced virtual sensors along the DAS cables lays in the fact that under ideal spatially white-noise conditions of non-correlated noise between the virtual DAS sensors, even sub-Nyquist spaced DAS sensors will increase the array white-noise gain, as shown by Equation S18 in Supporting Information S1. Still, a key limitation in array signal processing for real-world wavefields is that the noise is not necessarily spatially white but is also partly correlated between sensors. Moreover, the seismic signal wavefield coherence generally decreases with increased sensor separation, in particular when waves propagate in complex inhomogeneous media. Naturally, this is a key constraint for the maximum useful aperture size when designing seismic arrays (Gibbons, 2014; Mykkeltveit et al., 1983; Mykkeltveit, Fyen, et al., 1990).

These signal-decorrelation and noise-correlation effects can be taken into account when estimating the array gain following the recipe in Section S8 of Supporting Information S1. Regarding these aspects, we note that van den Ende and Ampuero (2021) observed a signal decorrelation over the DAS array which was larger than for conventional sensors and we call upon further studies on the signal coherence in real-world deployments and for various DAS signal processing settings. In array signal processing, there are several beamforming approaches based on maximizing the cross-correlation between the signal traces, rather than maximizing the beamformer output, when

determining the dominating horizontal slowness of an impinging wavefield (e.g., Gibbons et al., 2018; Ruigrok et al., 2017). Such approaches can be seen as performing a trace normalization before estimating the spatial covariance matrix **R** (see Section S5 of Supporting Information S1). This may to an extent compensate for the direction-dependent virtual element sensitivity of a DAS cable.

The current work does not provide rules for DAS array layout design, but we analyze a set of aspects that can be taken into account when elaborating such design rules based on the steered responses. In Section 4.2, we first visualized the steered responses as function of impinging wave slowness for a set of simplified DAS layouts, illustrating the effect of DAS sensor directivity on the steered response. Given its co-located conventional and DAS cable arrays, the NORES array in southeastern Norway is a suitable laboratory for the analysis of DAS array properties. The NORES DAS array consists of a set of cable "arms" stretching out from the array center. In Section 4.3, the steered response was assessed for each of the cable arms for a given direction of arrival. It was found that when the full DAS layout is exploited, its steered response for the direction-of-arrival set of interest will be comparable to the associated array response of the NORES conventional seismic array. Now further discussing the NORES DAS array and analyzing the calculated steered responses for all $\mathbf{s}_0$ of a given grid, Figure 10 provides a set of consolidated displays summarizing key parameters derived from the calculated steered response. It shows steered response characteristics estimated for the NORES DAS array geometry. First, it compares the mainlobe average width, and compares this to a triangular and to a spiral shaped DAS array of similar aperture size. We also estimate and display the mainlobe-to-sidelobe ratio for all directions-of-arrival over a given slowness grid, calculated using the following recipe: (a) For each single horizontal slowness grid point (which corresponds to a single direction-of-arrival), we calculate the steered response over the horizontal slowness grid; (b) From the steered response we extract the total mainlobe energy as well as the energy outside of the mainlobe – here for simplicity denoted sidelobe energy; (c) The ratio between mainlobe and sidelobe energy is calculated. The mainlobe energy, its average width, and the corresponding mainlobe-to-sidelobe ratio are then plotted for impinging waves with slowness given by the horizontal slowness grid. For source directions not well probed due to a narrow aperture, a larger mainlobe is naturally expected. For directions perpendicular to regions where the array layout is not sufficiently sampled in space, grating lobes appear and the mainlobe-to-sidelobe energy decreases (see also Sections S4 and S6 in Supporting Information S1). All in all, the analyzed triangular, spiral, and NORES experimental DAS geometries feature comparable performance in this steered-response based analysis. Still, the spiral array features the most homogeneous properties in terms of mainlobe width and mainlobe-to-sidelobe ratio as function of backazimuth. The NORES DAS layout also features quite equal steered response mainlobe width and mainlobe-to-sidelobe ratio direction of arrival, although the performance is slightly degraded for waves impinging approximately from the northwest. The triangle layout features poor mainlobe-to-sidelobe ratio for vertical arrival, for the three bands of backazimuths where the cable directivity and the array layout interplay to give a reduced ratio. The spiral layout shows a dipole of reduced mainlobe-to-sidelobe ratio for NW–SE directions, while the NORES cable layout gives high mainlobe-to-sidelobe ratio for NE–SW directions. The bottom row of Figure 10 displays the beamwidth as function of horizontal slowness. The triangular layout features three distinct lines of narrow beamwidth (i.e., high slowness resolution). These are aligned with directions perpendicular to the axis of the triangle legs. The spiral features best resolution in the NW–SE directions. In contrast, the NORES DAS layout mostly features high resolution for all slownesses, with only a minor region of wider mainlobe width in slownesses corresponding to steep arrivals from NE. In Section S9 of Supporting Information S1, we discuss and analyze additional aspects regarding DAS array design and provide further elaborations regarding the NORES DAS array.

The current study has focused on DAS array directional sensitivity to particle displacement, and the analysis is most straightforwardly mapped to P-wave arrivals. The strain sensitivity pattern observed on an array in the horizontal plane depends largely on the horizontal projections of their propagation and polarization vectors (Martin, 2018). When these are aligned (i.e., wave motion is in the direction of propagation) as in P, SV and Rayleigh waves we expect maximum sensitivity in-line. Conversely, when they are orthogonal as in SH and Love waves, we expect maximum sensitivity in the directions bisecting them (i.e., at $\pm 45°$ from the propagation direction) with alternating signs (e.g., Baird et al., 2020). Prospective future studies are in expanding the current study to S-, Rayleigh, and Love waves. This would also include elaborations regarding SH- and SV-wave polarization.

The frameworks developed can be applied in further studies where combinations of conventional, borehole, and DAS arrays are elaborated, providing guidance toward optimal cost-benefit in DAS array design. The paper has

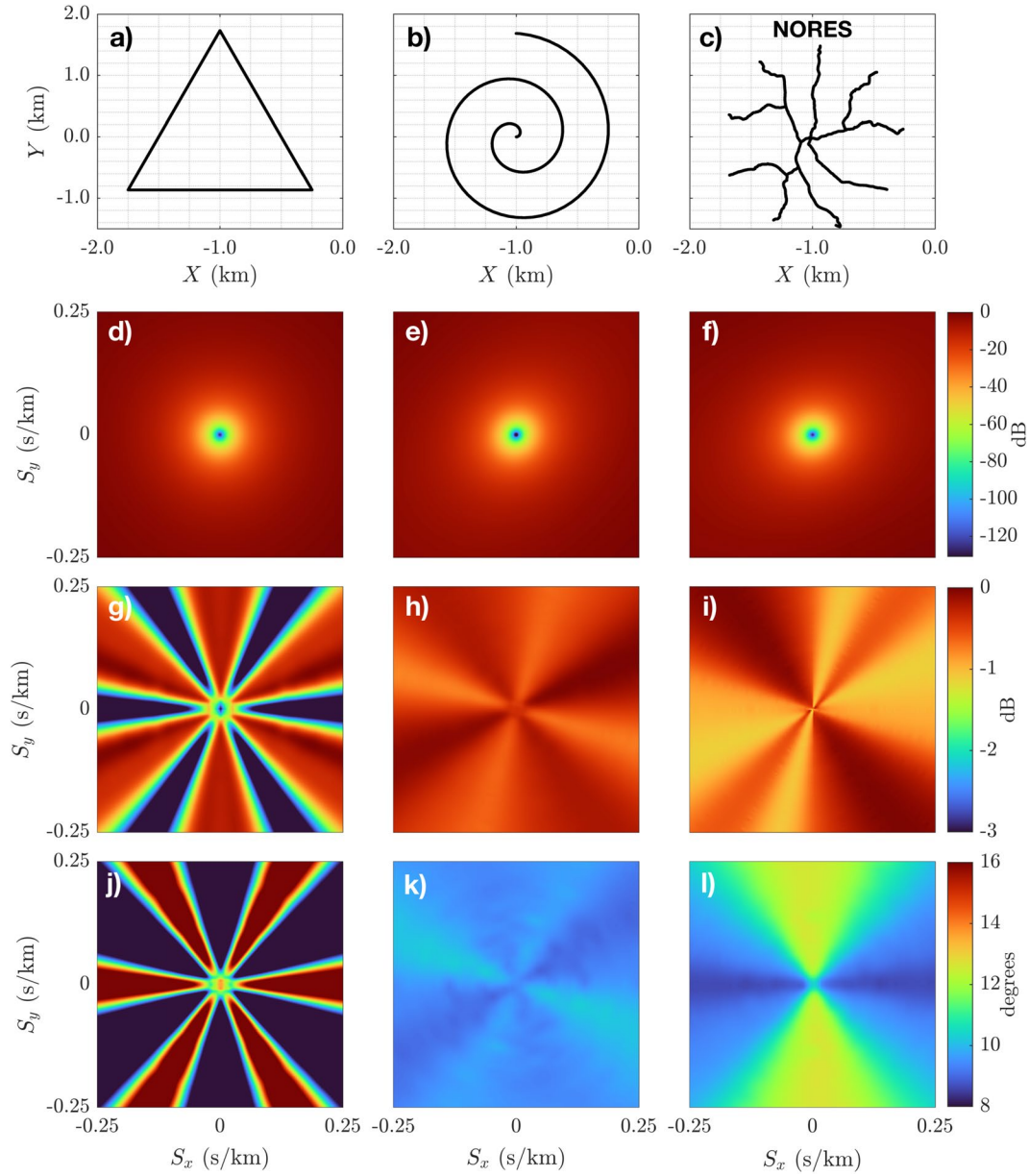

Figure 10. Consolidated steered response comparisons, evaluated on a [−0.25, 0.25] s/km slowness range grid and velocity 3.5 km/s, for 100 m gauge length. The virtual sources are located in the far-field and the analysis is performed at 20 Hz. Fiber cable layout geometries: (a) triangular DAS, (b) spiral DAS, (c) NORES DAS. Second row: Sensitivity distribution in terms of total steered response power as function of horizontal slowness for (d) triangular, (e) spiral, and (f) NORES DAS geometries. This is lowest when wavefront crosses the fiber array vertically and highest when the wavefront impinges horizontally. Third row: mainlobe-to-sidelobe energy ratio (for sidelobes down to 30 dB below the maximum mainlobe level), for (g) triangular, (h) spiral, (i) NORES DAS geometries. Fourth row: average beamwidth for (j) triangular, (k) spiral, (l) NORES DAS geometries. For the triangular DAS, the mainlobe-to-sidelobe energy ratio and beamwidth varies depending on the angular difference between impinging wavefront and triangle edge. The mainlobe-to-sidelobe ratio is highest for waves crossing the array at an angle of 30° and its multiples, while lowest at 60° and its multiples whereas, for the beamwidth this is reversed. Symmetrical response is also observed for the spiral layout although with less variation because of better azimuthal coverage. For NORES, the highest mainlobe-to-sidelobe energy is observed in north-west to south-east direction whereas the smallest beamwidth is in the east-west direction.

sought to convey concepts and nomenclature from array signal processing to the DAS community. Likewise, for an array signal processing expert audience, the ambition is that we have provided an accessible description of fundamental DAS concepts. Prospectively, the current work can help paving the way for cross-pollination of ideas

between these complimentary fields that can lead to new discoveries, enhanced signal processing, and optimized array designs for DAS applications and enhanced wavefield probing.

Data Availability Statement

The Supporting Information includes a textfile table with the layout for each of the NORES 9-arm fiber-optic cables (see also Section 4.3 and Figure 9). The NORES conventional sensor coordinates are available from Schweitzer et al. (2021).

Acknowledgments
SPN acknowledges partial support by the project Middle Atmosphere Dynamics: Exploiting Infrasound Using a Multi-disciplinary Approach at High Latitudes (MADEIRA), funded by the Research Council of Norway basic research programme FRIPRO/FRINATEK under Contract No. 274377. The authors are thankful for reviews received from David Bowden and an anonymous referee. These have without doubt helped us to produce an improved manuscript. The authors thank Tormod Kværna for discussions and valuable feedback that improved this work and Ekaterina Vorobeva for sharing her steered response calculation code.

References

Ajo-Franklin, J. B., Dou, S., Lindsey, N. J., Monga, I., Tracy, C., Robertson, M., et al. (2019). Distributed acoustic sensing using dark fiber for near-surface characterization and broadband seismic event detection. *Scientific Reports*, *9*(1), 1328. https://doi.org/10.1038/s41598-018-36675-8

Aki, K., & Richards, P. G. (2009). *Quantitative seismology* (2 Ed.). University Science Books.

Baird, A. (2020). Modelling the response of helically wound das cables to microseismic arrivals. In *First EAGE workshop on fibre optic sensing* (Vol. 1, pp. 1–5). European Association of Geoscientists & Engineers. https://doi.org/10.3997/2214-4609.202030019

Baird, A. F., Stork, A. L., Horne, S. A., Naldrett, G., Kendall, J.-M., Wookey, J., et al. (2020). Characteristics of microseismic data recorded by distributed acoustic sensing systems in anisotropic media. *Geophysics*, *85*(4), Ks139–Ks147. https://doi.org/10.1190/geo2019-0776.1

Bóna, A., Dean, T., Correa, J., Pevzner, R., Tertyshnikov, K., & Van Zaanen, L. (2017). Amplitude and phase response of DAS receivers. In *79th EAGE Conference and Exhibition 2017* (Vol. 1, pp. 1–5). European Association of Geoscientists & Engineers. https://doi.org/10.3997/2214-4609.201701200

Bowden, D. C., Klaasen, S., Martin, E., Paitz, P., & Fichtner, A. (2021). Wave-selective beamforming with distributed acoustic sensing. In *EGU General Assembly 2021*, EGU21-12216. European Geophysical Union. https://doi.org/10.5194/egusphere-egu21-12216

Capon, J. (1969). High-resolution frequency-wavenumber spectrum analysis. *Proceedings of the IEEE*, *57*(8), 1408–1418. https://doi.org/10.1109/proc.1969.7278

Chambers, K. (2020). Using DAS to investigate traffic patterns at Brady hot springs, Nevada, USA. *The Leading Edge*, *39*(11), 819–827. https://doi.org/10.1190/tle39110819.1

Costley, R. D., Frazier, W. G., Dillion, K., Picucci, J. R., Williams, J. E., & McKenna, M. H. (2013). Frequency-wavenumber processing for infrasound distributed arrays. *Journal of the Acoustical Society of America*, *134*(4), EL307–EL313. https://doi.org/10.1121/1.4818940

Dahlman, O., Mackby, J., Mykkeltveit, S., & Haak, H. (2011). *Detect and deter: Can Countries Verify the nuclear test ban?*. Springer Science & Business Media.

Daley, T., Miller, D., Dodds, K., Cook, P., & Freifeld, B. (2016). Field testing of modular borehole monitoring with simultaneous distributed acoustic sensing and geophone vertical seismic profiles at citronelle, Alabama. *Geophysical Prospecting*, *64*(5), 1318–1334. https://doi.org/10.1111/1365-2478.12324

Dean, T., & Correa, J. (2017). The determination of the seismic quality factor Q from VSP data acquired using distributed acoustic sensing. In *79th EAGE conference and Exhibition 2017*. EAGE Publications BV. https://doi.org/10.3997/2214-4609.201701203

Dean, T., Cuny, T., & Hartog, A. H. (2017). The effect of gauge length on axially incident P-waves measured using fibre optic distributed vibration sensing. *Geophysical Prospecting*, *65*(1), 184–193. https://doi.org/10.1111/1365-2478.12419

Dou, S., Lindsey, N., Wagner, A. M., Daley, T. M., Freifeld, B., Robertson, M., et al. (2017). Distributed acoustic sensing for seismic monitoring of the near surface: A traffic-noise interferometry case study. *Scientific Reports*, *7*(1), 11620. https://doi.org/10.1038/s41598-017-11986-4

Gal, M., Reading, A., Ellingsen, S., Koper, K., Gibbons, S., & Näsholm, S. (2014). Improved implementation of the fk and Capon methods for array analysis of seismic noise. *Geophysical Journal International*, *198*(2), 1045–1054. https://doi.org/10.1093/gji/ggu183

Gibbons, S. J. (2014). The applicability of incoherent array processing to IMS seismic arrays. *Pure and Applied Geophysics*, *171*(3), 377–394. https://doi.org/10.1007/s00024-012-0613-2

Gibbons, S. J., Asming, V., Eliasson, L., Fedorov, A., Fyen, J., Kero, J., et al. (2015). The European Arctic: A laboratory for seismoacoustic studies. *Seismological Research Letters*, *86*(3), 917–928. https://doi.org/10.1785/0220140230

Gibbons, S. J., Kværna, T., & Mykkeltveit, S. (2015). Could the IMS infrasound stations support a global network of small aperture seismic arrays? *Seismological Research Letters*, *86*(4), 1148–1159. https://doi.org/10.1785/0220150068

Gibbons, S. J., Näsholm, S. P., Ruigrok, E., & Kværna, T. (2018). Improving slowness estimate stability and visualization using limited sensor pair correlation on seismic arrays. *Geophysical Journal International*, *213*(1), 447–460. https://doi.org/10.1093/gji/ggx550

Gibbons, S. J., Ringdal, F., & Kværna, T. (2008). Detection and characterization of seismic phases using continuous spectral estimation on incoherent and partially coherent arrays. *Geophysical Journal International*, *172*(1), 405–421. https://doi.org/10.1111/j.1365-246x.2007.03650.x

Hudson, T. S., Baird, A. F., Kendall, J. M., Kufner, S. K., Brisbourne, A. M., Smith, A. M., et al. (2021). Distributed acoustic sensing (DAS) for natural microseismicity studies: A case study from Antarctica. *Journal of Geophysical Research: Solid Earth*, *126*. https://doi.org/10.1029/2020JB021493

Jerkins, A. E., Shiddiqi, H. A., Kværna, T., Gibbons, S. J., Schweitzer, J., Ottemöller, L., & Bungum, H. (2020). The 30 June 2017 north Sea earthquake: Location, characteristics, and context. *Bulletin of the Seismological Society of America*, *110*(2), 937–952. https://doi.org/10.1785/0120190181

Johnson, D. H., & Dudgeon, D. E. (1992). *Array signal processing: Concepts and techniques*. Simon & Schuster, Inc.

Jousset, P., Reinsch, T., Ryberg, T., Blanck, H., Clarke, A., Aghayev, R., et al. (2018). Dynamic strain determination using fibre-optic cables allows imaging of seismological and structural features. *Nature Communications*, *9*(1), 1–11. https://doi.org/10.1038/s41467-018-04860-y

Juarez, J. C., & Taylor, H. F. (2007). Field test of a distributed fiber-optic intrusion sensor system for long perimeters. *Applied Optics*, *46*(11), 1968–1971. https://doi.org/10.1364/AO.46.001968

Kennett, B., Stipčević, J., & Gorbatov, A. (2015). Spiral-arm seismic arrays. *Bulletin of the Seismological Society of America*, *105*(4), 2109–2116. https://doi.org/10.1785/0120140354

Klaasen, S., Paitz, P., Lindner, N., Dettmer, J., & Fichtner, A. (2021). Distributed acoustic sensing in volcano-glacial environments—Mount meager, British Columbia. *Journal of Geophysical Research: Solid Earth*, *126*(11), e2021JB022358. https://doi.org/10.1029/2021JB022358

Krim, H., & Viberg, M. (1996). Two decades of array signal processing research: The parametric approach. *IEEE Signal Processing Magazine*, *13*(4), 67–94. https://doi.org/10.1109/79.526899

Kuvshinov, B. (2016). Interaction of helically wound fibre-optic cables with plane seismic waves. *Geophysical Prospecting*, *64*(3), 671–688. https://doi.org/10.1111/1365-2478.12303

Kvaerna, T., & Doornbos, D. (1986). An integrated approach to slowness analysis with arrays and three-component stations, semiannual technical summary, 1 Apr.–30 Sept. 1986, NORSAR Sci. Rep, Tech. rep, No 2-85/86.

Kvaerna, T., Gibbons, S. J., & Näsholm, S. P. (2021). CTBT seismic monitoring using coherent and incoherent array processing. *Journal of Seismology*, *25*, 1189–1207. https://doi.org/10.1007/s10950-021-10026-z

Kværna, T. (1989). On exploitation of small-aperture noress type arrays for enhanced P-wave detectability. *Bulletin of the Seismological Society of America*, *79*(3), 888–900.

Lior, I., Sladen, A., Rivet, D., Ampuero, J.-P., Hello, Y., Becerril, C., et al. (2021). On the detection capabilities of underwater distributed acoustic sensing. *Journal of Geophysical Research: Solid Earth*, *126*(3), e2020JB020925. https://doi.org/10.1029/2020JB020925

Martin, E. R. (2018). *Passive imaging and characterization of the subsurface with distributed acoustic sensing*. Ph.D. thesisStanford University.

Martin, E. R., Lindsey, N. J., Ajo-Franklin, J. B., & Biondi, B. L. (2021). *Introduction to interferometry of fiber-optic strain measurements*. chap. 9 (pp. 111–129). American Geophysical Union (AGU). https://doi.org/10.1002/9781119521808.ch9

Mateeva, A., Lopez, J., Potters, H., Mestayer, J., Cox, B., Kiyashchenko, D., et al. (2014). Distributed acoustic sensing for reservoir monitoring with vertical seismic profiling. *Geophysical Prospecting*, *62*(4), 679–692. https://doi.org/10.1111/1365-2478.12116

Mykkeltveit, S., Åstebøl, K., Doornbos, D., & Husebye, E. (1983). Seismic array configuration optimization. *Bulletin of the Seismological Society of America*, *73*(1), 173–186.

Mykkeltveit, S., Fyen, J., Ringdal, F., & Kværna, T. (1990). Spatial characteristics of the noress noise field and implications for array detection processing. *Physics of the Earth and Planetary Interiors*, *63*(3–4), 277–283. https://doi.org/10.1016/0031-9201(90)90028-v

Mykkeltveit, S., Ringdal, F., Kværna, T., & Alewine, R. W. (1990). Application of regional arrays in seismic verification research. *Bulletin of the Seismological Society of America*, *80*(6B), 1777–1800.

Nayak, A., Ajo-Franklin, J., & the Imperial Valley Dark Fiber Team. (2021). Distributed acoustic sensing using dark fiber for array detection of regional earthquakes. *Seismological Research Letters*. https://doi.org/10.1785/0220200416

Oye, V., Dando, B., Wuestefeld, A., Jerkins, A., & Koehler, A. (2021). Cost-effective baseline studies for induced seismicity monitoring related to CO_2 storage site preparation. In *Proceedings of the 15th Greenhouse Gas Control Technologies Conference 15–18 March 2021*. https://doi.org/10.2139/ssrn.3819173

Paitz, P., Sager, K., & Fichtner, A. (2019). Rotation and strain ambient noise interferometry. *Geophysical Journal International*, *216*(3), 1938–1952. https://doi.org/10.1093/gji/ggy528

Peng, F., Duan, N., Rao, Y., & Li, J. (2014). Real-time position and speed monitoring of trains using phase-sensitive otdr. *IEEE Photonics Technology Letters*, *26*(20), 2055–2057. https://doi.org/10.1109/LPT.2014.2346760

Rodriguez, I. V., & Wuestefeld, A. (2020). Strain microseismics: Radiation patterns, synthetics, and moment tensor resolvability with distributed acoustic sensing in isotropic media. *Geophysics*, *85*(3), KS101–KS114. https://doi.org/10.1190/geo2019-0373.1

Rost, S., & Thomas, C. (2002). Array seismology: Methods and applications. *Reviews of Geophysics*, *40*(3), 2–1. https://doi.org/10.1029/2000rg000100

Rost, S., & Thomas, C. (2009). Improving seismic resolution through array processing techniques. *Surveys in Geophysics*, *30*(4–5), 271–299. https://doi.org/10.1007/s10712-009-9070-6

Ruigrok, E., Gibbons, S., & Wapenaar, K. (2017). Cross-correlation beamforming. *Journal of Seismology*, *21*(3), 495–508. https://doi.org/10.1007/s10950-016-9612-6

Schweitzer, J. (2014). Seismometer arrays. In M. Beer, I. A. Kougioumtzoglou, E. Patelli, & I. S.-K. Au (Eds.), *Encyclopedia of earthquake Engineering* (pp. 1–11). Springer Berlin Heidelberg. https://doi.org/10.1007/978-3-642-36197-5_191-1

Schweitzer, J., Fyen, J., Mykkeltveit, S., Gibbons, S. J., Pirli, M., Kühn, D., & Kvaerna, T. (2012). Seismic arrays. In P. Bormann (Ed.), *New manual of seismological observatory practice 2 (NMSOP-2)* (pp. 1–80). Deutsches GeoForschungsZentrum GFZ. https://doi.org/10.2312/GFZ.NMSOP-2_CH9

Schweitzer, J., Köhler, A., & Christensen, J. M. (2021). Development of the NORSAR network over the last 50 yr. *Seismological Society of America*, *92*(3), 1501–1511. https://doi.org/10.1785/0220200375

Smith, S. W. (1997). *The Scientist and Engineer's guide to Digital signal processing*. California Technical Publishing. Retrieved from www.dspguide.com

Tejedor, J., Macias-Guarasa, J., Martins, H. F., Piote, D., Pastor-Graells, J., Martin-Lopez, S., et al. (2017). A novel fiber optic based surveillance system for prevention of pipeline integrity threats. *Sensors*, *17*(2), 355. https://doi.org/10.3390/s17020355

Uncini, A. (2015). *Discrete space-time filtering* (pp. 477–578). Springer International Publishing. https://doi.org/10.1007/978-3-319-02807-1_9

van den Ende, M. P. A., & Ampuero, J.-P. (2021). Evaluating seismic beamforming capabilities of distributed acoustic sensing arrays. *Solid Earth*, *12*(4), 915–934. https://doi.org/10.5194/se-12-915-2021

van Trees, H. L. (2004). *Optimum array processing: Part IV of detection, estimation, and modulation theory*.

Waagaard, O. H., Rønnekleiv, E., Haukanes, A., Stabo-Eeg, F., Thingbø, D., Forbord, S., et al. (2021). Real-time low noise distributed acoustic sensing in 171 km low loss fiber. *OSA Continuum*, *4*(2), 688–701. https://doi.org/10.1364/OSAC.408761

Walter, F., Gräff, D., Lindner, F., Paitz, P., Köpfli, M., Chmiel, M., & Fichtner, A. (2020). Distributed acoustic sensing of microseismic sources and wave propagation in glaciated terrain. *Nature Communications*, *11*(1), 1–10. https://doi.org/10.1038/s41467-020-15824-6

Ward, J., Thorne, M., Nowacki, A., & Rost, S. (2021). Automatic slowness vector measurements of seismic arrivals with uncertainty estimates using bootstrap sampling, array methods and unsupervised learning. *Geophysical Journal International*, *226*(3), 1847–1857. https://doi.org/10.1093/gji/ggab196

Williams, E. F., Fernández-Ruiz, M. R., Magalhaes, R., Vanthillo, R., Zhan, Z., González-Herráez, M., & Martins, H. F. (2019). Distributed sensing of microseisms and teleseisms with submarine dark fibers. *Nature Communications*, *10*(1), 5778. https://doi.org/10.1038/s41467-019-13262-7

Wuestefeld, A., & Wilks, M. (2019). How to twist and turn a fiber: Performance modeling for optimal DAS acquisitions. *The Leading Edge*, *38*(3), 226–231. https://doi.org/10.1190/tle38030226.1

Zhan, Z. (2020). Distributed acoustic sensing turns fiber-optic cables into sensitive seismic antennas. *Seismological Research Letters*, *91*(1), 1–15. https://doi.org/10.1785/0220190112

Zhan, Z., Cantono, M., Kamalov, V., Mecozzi, A., Müller, R., Yin, S., & Castellanos, J. C. (2021). Optical polarization-based seismic and water wave sensing on transoceanic cables. *Science*, *371*(6532), 931–936. https://doi.org/10.1126/science.abe6648

Zhao, Y., & Li, Y. E. (2020). On beamforming of ambient noise recorded by DAS. In *SEG Technical Program expanded Abstracts 2020* (pp. 515–519). Society of Exploration Geophysicists. https://doi.org/10.1190/segam2020-3425427.1

Zhu, T., & Stensrud, D. J. (2019). Characterizing thunder-induced ground motions using fiber-optic distributed acoustic sensing array. *Journal of Geophysical Research: Atmospheres*, *124*, 12810–12823. https://doi.org/10.1029/2019JD031453

Zumberge, M. A., Berger, J., Hedlin, M. A. H., Husmann, E., Nooner, S., Hilt, R., & Widmer-Schnidrig, R. (2003). An optical fiber infrasound sensor: A new lower limit on atmospheric pressure noise between 1 and 10 Hz. *Journal of the Acoustical Society of America*, *113*(5), 2474–2479. https://doi.org/10.1121/1.1566978

References From the Supporting Information

Grythe, J. (2015). *Array gain and reduction of self-noise*, Technical Report. Norsonic AS.

Kito, T., & Krüger, F. (2001). Heterogeneities in D" beneath the southwestern Pacific inferred from scattered and reflected P-waves. *Geophysical Research Letters*, *28*(13), 2545–2548. https://doi.org/10.1029/2000gl012801